

# A One-dimensional Model of Blood Flow in Arteries with Friction and Convection Based on the Womersley Velocity Profile

Karim Azer · Charles S. Peskin

Published online: 14 June 2007  
© Springer Science+Business Media, LLC 2007

**Abstract** In this paper, we present a one-dimensional model for blood flow in arteries, without assuming an a priori shape for the velocity profile across an artery (Azer, Ph.D. thesis, Courant Institute, New York University, 2006). We combine the one-dimensional equations for conservation of mass and momentum with the Womersley model for the velocity profile in an iterative way. The pressure gradient of the one-dimensional model drives the Womersley equations, and the velocity profiles calculated then feed back into both the friction and nonlinear parts of the one-dimensional model. Besides enabling us to evaluate the friction correctly and also to use the velocity profile to correct the nonlinear terms, having the velocity profile available as output should be useful in a variety of applications. We present flow simulations using both structured trees and pure resistance models for the small arteries, and compare the resulting flow and pressure waves under various friction models. Moreover, we show how to couple the one-dimensional equations with the Taylor diffusion limit (Azer, *Int J Heat Mass Transfer* 2005;48:2735–40; Taylor, *Proc R Soc Lond Ser A* 1953;219:186–203) of the convection-diffusion equations to drive the concentration of a solute along an artery in time.

**Keywords** One-dimensional blood flow · Womersley · MRI · Shear stress · Velocity profile · Structured tree · Hypertension · Compliance · Taylor diffusion

K. Azer · C. S. Peskin  
Courant Institute of Mathematical Sciences, New York University, New York, NY, USA

K. Azer (✉)  
Applied Computer Science and Mathematics Department,  
RY 84-202, 126 E. Lincoln Ave., Rahway, NJ 07065, USA  
e-mail: Karim\_Azer@Merck.com

## Introduction

The goal of this work is to use a one-dimensional model to study the flow of blood through the arterial system. Our model allows us to solve for the flow and pressure waveforms at any point along the arterial tree, but also, as we shall see later, to solve for the velocity profile at any particular cross-section of an artery in the tree. These profiles respond to changes in the characteristics of the arterial tree, such as arterial wall compliance, in a way that distinguishes normal and abnormal behaviors.

Arteries are the means by which oxygenated blood is carried away from the heart and distributed to body tissue. Physiologically, blood flow through tissues and organs is largely determined by oxygen availability or demand through complex biochemical processes. Mechanically, blood flow is driven by the pressure gradient along the arterial tree, which serves primarily to accelerate or decelerate the flow in these low-resistance vessels (Hoppensteadt et al. 2002; Pedley 1980). The arterial tree is a complex system of vessels, branching at bifurcation points. The vessels are tapering, narrowing as one follows a vessel downstream away from the heart. The vessel walls are compliant, maintaining flow through them at all times. The compliant vessel walls store volume during systole and return that volume during diastole, thus maintaining a more nearly steady flow than would otherwise be the case. The total cross-sectional area of the aorta is about  $2.5 \text{ cm}^2$ , which then branches out to a total of approximately  $20 \text{ cm}^2$  at the level of the small arteries, and  $40 \text{ cm}^2$  at the level of the arterioles (Caro et al. 1978; Guyton and Hall 2000). Thus, at each bifurcation, the total cross-section of the daughter branches is greater than the cross-section of the parent branch, even though the cross-section of each individual daughter branch is less than that of the parent.

Flow through the arterial system is pulsatile, because of the beating of the heart, and is met with resistance at the distal ends of the arterial tree. This resistance is generated by the arterioles because of their small radii. Recall that resistance per unit length of a vessel depends inversely on the fourth power of the radius. It is for this reason that the total resistance per unit length can increase even though the total cross-sectional area of the arterial tree is also increasing as one travels away from the heart.

Studying blood flow in arteries and veins has many direct applications in medicine, including hypertension and atherosclerosis. Both of these conditions may develop in patients with diabetes. An early sign of diabetes is a change in the waveform of the arterial pulse: the disappearance of a secondary peak known as the dicrotic wave (Feinberg and Lax 1958; Lax et al. 1956). This was discovered by Henry Lax nearly 50 years ago. Accurate simulation of the arterial pulse is therefore important. Atherosclerosis is known to favor selectively arterial bends and bifurcations. Since flow at these locations is typically different from flow in relatively straight arterial sections, local hemodynamic factors, such as wall shear stress, have been widely accepted as important in disease initiation and progression (Caro et al. 1978). Being able to estimate wall shear stress is therefore important. Often, three-dimensional models are used when there is the need for computing the wall shear stress. When geometric effects are not the main interest, our one-dimensional model can be used, instead of a three-dimensional model to compute shear stress at the wall. This is because we use Womersley theory in conjunction with the one-dimensional model to obtain local, time-dependent velocity profiles. The main advantages of using a one-dimensional model are speed and ease of use, but also being able to simulate a complete arterial network as opposed to a small section of the tree. This enables one to study the changes in the wall shear stress in diseased arterial networks, as well as the wave propagation effects of arterial diseases such as atherosclerosis that are caused by stiffened arteries and other changes in vessel wall characteristics.

In principle, knowledge of the velocity profile allows one to compute the pressure and flow throughout an arterial tree more accurately because it enables more accurate evaluation of the frictional and nonlinear terms that appear in the one-dimensional theory. In practice, however, we find that the effects of the velocity profile on the propagation of the arterial pulse are small. Despite this, it is valuable to have the velocity profile available as output because it enables the calculation of the shear stress at the wall (which influences lipid transport and the pathogenesis of atherosclerosis), and also because it is needed for calculation of mass transport in arteries by time-dependent Taylor diffusion (Azer 2005), as we shall see in Sect.

“Taylor diffusion combined with blood flow simulation in a vessel”. An additional benefit of having the velocity profile available as output is that the velocity profile can be measured (e.g. by Doppler ultrasound or Magnetic Resonance Imaging) and this provides a sensitive check on a computational model.

We model blood flow in arteries (the same methodology is applicable to veins) by combining one-dimensional conservation laws with Womersley theory. The one-dimensional theory allows us to solve for the pressure and flow along an artery. Womersley theory gives the velocity profile, under the assumption that flow is independent of axial position along an artery. Even though these two theories might seem to be mismatched, they prove to work well together. In particular, the one-dimensional theory generates the pressure gradient that is needed as input to the Womersley theory, and the Womersley theory provides the velocity profile which is used in the computation of the friction and nonlinear terms of the one-dimensional theory. In this paper, we present a numerical algorithm for solving one-dimensional blood flow equations and show how to calculate velocity profiles, and also how to use the information from these profiles to get a better one-dimensional model of blood flow. We show that the algorithm is second order accurate and present a simulation based on experimental data from humans. We also present comparisons of flow and pressure computed using both structured tree (Olufsen et al. 2000) and simple resistance outflow boundary conditions, and under various friction models. The comparisons show that structured trees have superior properties when modeling flow in an arterial tree over a simple resistance method. Moreover, we apply our model to study the role of compliance in hypertension and show how compliance affects the pressure waveforms throughout the arterial tree. As an example of the importance of having the velocity profiles as output in our one-dimensional model, we also show how to couple our model equations with the equations of mass transport in an artery by unsteady Taylor diffusion (Azer 2005).

## Model Assumptions and Equations

### The One-dimensional Model

We use a one-dimensional system of hyperbolic partial differential equations derived from the Navier-Stokes equations together with a state equation for the vessel walls to model blood flow in the large arteries. We first assume that we have the velocity profile, and integrate the volume and momentum balance equations over the arterial cross-section to get a one-dimensional set of equations for blood flow through an arterial tree. The state equation describes

how the walls of the arteries behave under pressure. We assume that arteries are purely elastic and therefore do not take into consideration the viscoelastic nature of artery walls (Caro et al. 1978). We also assume that blood is incompressible and Newtonian. Let  $x$  be the distance along the artery,  $r$  denote radial position,  $t$  denote time,  $v(r, x, t)$  be the axial velocity of blood,  $A(x, t)$  denote the cross-sectional area,  $p(x, t)$  be the pressure inside the artery wall with respect to outside,  $f(x, t)$  be the friction force exerted by the vessel wall on the blood per unit volume of blood contained within the vessel, and let  $\rho$  be the density, which we take to be constant. Let

$$V(t; x_1, x_2) = \int_{x_1}^{x_2} A(x, t) dx \quad (1)$$

be the volume of fluid in the segment of the arterial tube between  $x = x_1$  and  $x = x_2$ . Also let

$$M(t; x_1, x_2) = \int_{x_1}^{x_2} \rho \left( 2\pi \int_0^{R(x, t)} v(r, x, t) r dr \right) dx \quad (2)$$

be the axial momentum of the fluid between  $x_1$  and  $x_2$ . It follows that

$$\frac{\partial V}{\partial t} = \int_{x_1}^{x_2} \frac{\partial A}{\partial t} dx \quad (3)$$

$$\frac{\partial M}{\partial t} = 2\pi\rho \int_{x_1}^{x_2} \frac{\partial}{\partial t} \left( \int_0^{R(x, t)} v(r, x, t) r dr \right) dx. \quad (4)$$

Moreover, since the rate of change of volume of the tube segment between  $x_1$  and  $x_2$  is equal to the flow in at  $x_1$  minus the flow out at  $x_2$ , we can also write the rate of change of volume as

$$\begin{aligned} \frac{\partial V}{\partial t} &= -2\pi \int_0^{R(x_1, t)} v(r, x_1, t) r dr \Big|_{x_1}^{x_2} = -2\pi \int_{x_1}^{x_2} \frac{\partial}{\partial x} \\ &\times \left( \int_0^{R(x, t)} v(r, x, t) r dr \right) dx \end{aligned} \quad (5)$$

where we have used the fundamental theorem of calculus to convert a difference to the integral of a derivative. It therefore follows by comparing Eqs. 3 and 5 that

$$\int_{x_1}^{x_2} \frac{\partial A}{\partial t} dx = -2\pi \int_{x_1}^{x_2} \frac{\partial}{\partial x} \left( \int_0^{R(x, t)} v(r, x, t) r dr \right) dx \quad (6)$$

Rearranging, simplifying and making use of the arbitrariness of  $x_1$  and  $x_2$ , we get the following equation for conservation of volume:

$$\frac{\partial A}{\partial t} + \frac{\partial(uA)}{\partial x} = 0 \quad (7)$$

where

$$u(x, t) = \frac{2\pi}{A} \int_0^{R(x, t)} v(r, x, t) r dr \quad (8)$$

is the mean axial velocity of blood.

Now we derive the conservation of momentum equation. The rate of change, with respect to time, of the axial momentum of the fluid in the segment of the tube between  $x_1$  and  $x_2$  is equal to the net rate at which axial momentum is transported into that segment of tubing plus the net axial force acting upon the fluid within that segment. The axial force is applied by the pressure acting across the planes  $x = x_1$  and  $x = x_2$ , by the pressure applied along the tapered walls of the vessel between  $x_1$  and  $x_2$ , and by the friction force at the wall between  $x_1$  and  $x_2$ . These considerations lead to the following equation:

$$\begin{aligned} \frac{\partial M}{\partial t} &= - \int_0^{R(x_1, t)} (\rho v(r, x_1, t) (2\pi r dr) v(r, x_1, t)) \Big|_{x=x_1}^{x_2} - (pA) \Big|_{x=x_1}^{x_2} \\ &+ \int_{x_1}^{x_2} p \frac{\partial A}{\partial x} dx + \int_{x_1}^{x_2} \mu \frac{\partial v}{\partial r} (2\pi R(x, t)) dx \end{aligned} \quad (9)$$

In the momentum transport term,  $\rho v$  is the axial momentum per unit volume of fluid, and  $(2\pi r dr) v$  is the volume per unit time entering or leaving the segment of tube between  $x = x_1$  and  $x = x_2$  through the annulus defined by  $(r, r + dr)$ . The term  $\int_{x_1}^{x_2} p \frac{\partial A}{\partial x} dx$  is the contribution of the tube walls to the total axial force acting on the fluid between  $x = x_1$  and  $x = x_2$ . It is obtained by projecting the normal force  $-\int_{x_1}^{x_2} p \underline{n} dS$  onto the axial direction, where  $\underline{n}$  is the outward unit normal to the tube and  $dS$  is the area element. If  $\underline{a}$  is a constant unit vector in the axial direction, then the force that we want is  $-\int_{x_1}^{x_2} p(\underline{n} \cdot \underline{a}) dS$ . From the geometry of a tapered tube,  $-(\underline{n} \cdot \underline{a}) dS = dA = \frac{\partial A}{\partial x} dx$ . The term  $\int_{x_1}^{x_2} \mu \frac{\partial v}{\partial r} (2\pi R(x, t)) dx$  is the viscous contribution to the axial force acting on the fluid between  $x = x_1$  and  $x = x_2$ . The shear stress at the wall at a given location along the axis of the tube is given by  $\mu \frac{\partial v}{\partial r}$ . The product of the surface area element  $2\pi R(x, t) dx$  with the shear stress, integrated over the length of the tube section, gives the total friction force acting on the fluid between  $x = x_1$  and  $x = x_2$ .

Again using the fundamental theorem of calculus as in the derivation of Eq. 5, we see that Eq. 9 is equivalent to

$$\begin{aligned} \frac{\partial M}{\partial t} &= \int_{x_1}^{x_2} \left( -\frac{\partial}{\partial x} \left( pA + 2\pi\rho \int_0^{R(x, t)} v(r, x, t)^2 r dr \right) \right. \\ &\left. + p \frac{\partial A}{\partial x} + 2\pi R(x, t) \mu \frac{\partial v}{\partial r} \right) dx \end{aligned} \quad (10)$$

Comparing Eqs. 4 and 10, making use of the arbitrariness of  $x_1$  and  $x_2$ , and simplifying, we get the following form of the momentum equation:

$$\rho \left( \frac{\partial}{\partial t} (uA) + \frac{\partial}{\partial x} (wA) \right) + A \frac{\partial p}{\partial x} = fA \quad (11)$$

where

$$w = \frac{2\pi}{A} \int_0^{R(x,t)} (v(r, x, t))^2 r dr \quad (12)$$

and

$$f = \frac{2}{R} \mu \frac{\partial v(R(x, t), x, t)}{\partial r} \quad (13)$$

Note that  $f(x, t)$  is the frictional force per unit volume of blood exerted by the walls of the vessel on the flowing blood that is contained within a short segment of vessel length  $\Delta x$  near  $x$ . The force per unit area of wall is  $\mu \frac{\partial v}{\partial r}$ , and this is multiplied by the area of wall per unit volume of blood within the vessel, namely  $\frac{2\pi R \Delta x}{\pi R^2 \Delta x} = \frac{2}{R}$ .

By combining Eqs. 7 and 11, we can derive the following form of the momentum equation

$$\frac{\partial u}{\partial t} + u \frac{\partial u}{\partial x} + \frac{1}{\rho} \frac{\partial p}{\partial x} = \frac{1}{A} \frac{\partial (A(u^2 - w))}{\partial x} + \frac{f}{\rho} \quad (14)$$

Note that

$$A(u^2 - w) = 2\pi \int_0^{R(x,t)} (v(r, x, t) - u(x, t))^2 r dr \quad (15)$$

which is a measure of the deviation of the actual velocity profile  $v(r, x, t)$  from the mean flat profile  $u(x, t)$ . The terms on the left in Eq. 14 are the terms one would get by assuming a flat profile (which would require zero viscosity, in order to allow for the slip at the walls which a flat profile implies). The effect of the actual profile appears on the right-hand side.

We consider pressure as a function of cross-sectional area  $A$ :

$$p = p(A)$$

Qualitatively, the “tube law”  $p(A)$  is a convex function, so that a given increase in cross-sectional area requires a greater increase in pressure when the pressure is high than when the pressure is low. The quantitative choice of  $p(A)$  will be stated in the Results section. The tube law plays the same role as the equation of state in gas dynamics. Differentiating the tube law, we get

$$\frac{\partial p}{\partial x} = p'(A) \frac{\partial A}{\partial x} \quad (16)$$

and Eq. 14 becomes

$$\rho \left( \frac{\partial u}{\partial t} + u \frac{\partial u}{\partial x} \right) + p'(A) \frac{\partial A}{\partial x} = \frac{\rho}{A} \frac{\partial (A(u^2 - w))}{\partial x} + f \quad (17)$$

Writing Eqs. 7 and 17 as a system, we have

$$\frac{\partial}{\partial t} \left( \frac{u}{A} \right) + \frac{\partial}{\partial x} \left( \frac{\frac{1}{2} u^2 + \frac{p(A)}{\rho}}{uA} \right) = \left( \frac{\frac{1}{A} \frac{\partial (A(u^2 - w))}{\partial x}}{0} + f \right) \quad (18)$$

### Womersley Theory: Estimating the Velocity Profile and its Effect on Both the Nonlinear and the Friction Terms

We use Womersley theory to calculate the velocity profile that is needed in the system of Eq. 18 and use the profile to include both friction and the nonlinear term in the model, without specifying any particular profile beforehand. The assumptions of the Womersley model are that we have an infinitely long rigid cylindrical vessel, that the flow is only in the axial  $x$  direction, and that there is no slip at the boundary of the artery (Nichols et al. 1998; Pedley 1980). The pressure gradient is an input to the Womersley theory and comes in our work from the 1D theory derived in the preceding section. Every  $x$ -position along an artery is thus idealized to be an infinitely long rigid tube for the purposes of calculating the velocity profile only. With these assumptions, Womersley derives the following partial differential equation for the profile of axial velocity  $v(y, z, t)$ :

$$\rho \frac{\partial v}{\partial t} - \mu \left( \frac{\partial^2}{\partial y^2} + \frac{\partial^2}{\partial z^2} \right) v = G_0(t) \quad (19)$$

with the boundary condition that  $v = 0$  on  $y^2 + z^2 = r_0^2$  where  $r_0$  is the radius of tube. This is the no slip condition. In Eq. 19,  $-G_0(t)$  is the local axial pressure gradient which we obtain from the 1D model.

To solve for  $v(y, z, t)$ , we let

$$G_0(t) = \sum_{-\infty}^{\infty} \hat{G}_k \exp(ik\omega_0 t) \quad (20)$$

where  $\omega_0 T = 2\pi$ , with  $T$  being the period of the heartbeat. Then we look for a solution of the form

$$v(y, z, t) = \sum_{-\infty}^{\infty} \hat{v}_k(r) \exp(ik\omega_0 t) \quad (21)$$

where  $r = \sqrt{y^2 + z^2}$ , in which the axial velocity profile has radial symmetry. Substituting 21 and 22 into 20 and collecting the coefficients of  $\exp(ik\omega_0 t)$ , we conclude that

$$-\mu \frac{\partial^2 \hat{v}_k}{\partial r^2} - \frac{\mu}{r} \frac{\partial \hat{v}_k}{\partial r} + ik\omega_0 \rho \hat{v}_k = \hat{G}_k \quad (22)$$

with the boundary condition

$$\hat{v}(r_0) = 0 \quad (23)$$

where  $r_0$  is the local radius of the artery. (In practice, we use the time averaged radius from the 1D theory for  $r_0$ .) Solving equation 22 subject to the boundary condition 23 we get

$$\hat{v}_k = \frac{i\hat{G}_k}{k\omega_0\rho} \left( -1 + \frac{J_0\left((1-i)r\sqrt{\frac{k\omega_0\rho}{2\mu}}\right)}{J_0\left((1-i)r_0\sqrt{\frac{k\omega_0\rho}{2\mu}}\right)} \right) \quad (24)$$

where  $J_0$  is the zeroth order Bessel function of the first kind. We then express the Bessel function  $J_0(r)$  in terms of its modulus and angle as follows (Nichols et al. 1998):

$$J_0(r) = M(r)e^{i\theta(r)} \quad (25)$$

Using 26 therefore gives the following expression for  $\hat{v}_k$ :

$$\hat{v}_k = \frac{-\hat{G}_k}{k\omega_0\rho} \frac{M(\alpha r)}{M_0} \sin(\theta(\alpha r) - \theta_0) + i \frac{\hat{G}_k}{k\omega\rho} \left( \frac{M(\alpha r)}{M_0 \cos(\theta(\alpha r) - \theta_0) - 1} \right). \quad (26)$$

where  $\alpha = (1-i)\sqrt{\frac{k\omega_0\rho}{2\mu}}$ . This formula allows us to evaluate  $\hat{v}_k(r)$  for as many values of  $k$  and  $r$  as may be needed, and then we can sum the Fourier series (with the help of the Fast Fourier Transform) to get  $v(r,t)$ . To evaluate the friction term, we also need  $\frac{\partial v}{\partial r}$  evaluated at the wall ( $r = r_0$ ). This is found by differentiating the right-hand side of equation 26 analytically with respect to  $r$ , evaluating the result at  $r = r_0$ , and then summing the Fourier series to obtain  $\frac{\partial v}{\partial r}$ . We can then compute the friction contribution as follows:

$$f = \frac{2\mu}{r} \frac{\partial v}{\partial r} \Big|_{r=r_0} \quad (27)$$

An interesting question that arises in matching the one-dimensional theory to the Womersley theory is whether to use the negative axial gradient of the static pressure,  $p$ , or of the dynamic pressure,  $p + \frac{1}{2}u^2$ , to drive the Womersley flow. From the standpoint of pure Womersley theory, it makes no difference which choice is made, since an infinitely long rigid tube has a velocity field that is the same at every  $x$ , so the axial gradient of  $u^2$  is zero in that case. In our case, however,  $u(x,t)$  comes from the solution of the one-dimensional equations of an *elastic* tube, and therefore  $u(x,t)$  has nontrivial dependence on the axial coordinate  $x$ . Thus  $\frac{\partial p}{\partial x} \neq \frac{\partial}{\partial x} \left( p + \frac{1}{2}u^2 \right)$ , and we have to decide which one to use. To address this, we start by using the Womersley equation with a pressure  $p_w$  to be determined

$$\rho \frac{\partial v}{\partial t} + \frac{\partial p_w}{\partial x} = \mu \Delta v \quad (28)$$

where

$$\Delta v = \frac{1}{r} \frac{\partial}{\partial r} \left( r \frac{\partial v}{\partial r} \right), \quad (29)$$

$v = v(r,t;x)$  denotes the Womersley velocity and  $p_w = p_w(x,t)$  will be determined from the one-dimensional pressure. It is important to keep in mind that  $p_w(x,t)$  is regarded as a known function when solving for the velocity profile  $v(r,t;x)$  at each  $x$ . Therefore, the term  $\frac{\partial p_w}{\partial x}$  is also regarded as known, even though it is yet to be determined from the one-dimensional model. It follows that the variable  $x$  plays only a parametric role in Eqs. 28 and 29, that is, the problem of solving for the velocity profile  $v(r,t;x)$  is a separate problem for each  $x$  in the present formulation.

Integrating equation 28 over the cross-section yields

$$\rho \frac{\partial Q}{\partial t} + \bar{A} \frac{\partial}{\partial x} p_w = \mu \int_0^{\bar{R}(x)} \Delta v (2\pi r) dr \quad (30)$$

where  $Q$  denotes the Womersley flow at a given  $x$  location,  $Q(t;x) = 2\pi \int_0^{\bar{R}(x)} v(r,t;x) r dr$ ,  $\bar{R}(x)$  is the mean over time of the radius at the point  $x$  and  $\bar{A} = \pi \bar{R}^2$ . Simplifying the integral on the right in equation 30:

$$\begin{aligned} \mu \int_0^{\bar{R}(x)} \Delta v (2\pi r) dr &= 2\pi \mu \int_0^{\bar{R}(x)} \frac{\partial}{\partial r} \left( r \frac{\partial v}{\partial r} \right) dr \\ &= 2\pi \mu \bar{R} \frac{\partial v}{\partial r} \Big|_{r=\bar{R}} = 2A \frac{\mu}{\bar{R}} \frac{\partial v}{\partial r} \Big|_{r=\bar{R}} \end{aligned} \quad (31)$$

We therefore have the following equation:

$$\rho \frac{\partial Q}{\partial t} + \bar{A} \frac{\partial}{\partial x} p_w = 2\bar{A} \frac{\mu}{\bar{R}} \frac{\partial v}{\partial r} \Big|_{r=\bar{R}} \quad (32)$$

If we let  $\bar{v} = \frac{Q}{\bar{A}}$ , we get that

$$\rho \frac{\partial \bar{v}}{\partial t} + \frac{\partial p_w}{\partial x} = f \quad (33)$$

where  $f$  is the friction term coming from the Womersley theory, and given by  $f = \frac{2\mu}{\bar{R}} \frac{\partial v}{\partial r} \Big|_{r=\bar{R}}$ . Recall that the 1D momentum equation is given by

$$\rho \frac{\partial u}{\partial t} + \frac{\partial}{\partial x} \left( p + \frac{1}{2} \rho u^2 \right) = f + \frac{1}{A} \frac{\partial (A(u^2 - w))}{\partial x} \quad (34)$$

Subtracting equation 33 from equation 34 we get that

$$\frac{\partial u}{\partial t} + \frac{\partial}{\partial x} \left( p + \frac{1}{2} \rho u^2 - p_w \right) = \frac{\partial \bar{v}}{\partial t} + \frac{1}{A} \frac{\partial (A(u^2 - w))}{\partial x} \quad (35)$$



In the case where  $u^2 = w$ , which is exactly true for the flat profile and approximately true in our results even when we do not assume a flat profile, we see that the correct choice of  $p_w$  is  $p_w = p + \frac{1}{2}u^2$ . With this choice of  $p_w$ , and in the case where  $u^2 = w$  equation 35 simplifies to

$$\frac{\partial u}{\partial t} = \frac{\partial \bar{v}}{\partial t} \quad (36)$$

To the extent that the approximation  $u^2 = w$  is correct, this shows that the use of the dynamic pressure to drive the Womersley flow has the result that the velocity averaged over a cross-section of the artery will be the same function of time in the Womersley theory as in the one-dimensional theory up to an unknown additive constant. We fix this additive constant by forcing the time averaged flow to agree in the two cases. By “flow” we mean the integral of the axial velocity over a cross-section of the artery. Note that the flow is the flux of a conserved quantity, the fluid volume. In order to achieve the matching of the time-averaged flow rates of the Womersley and one-dimensional computations, we discard the  $k = 0$  instance of equation 36 and replace it by the condition that the time-averaged flow rate of the Womersley solution should be the same as that of the corresponding one-dimensional flow. After a few cardiac cycle iterations, the one-dimensional flow and the Womersley flow of the artery match at every  $x$  location at any given time. We compared the matching of the one-

dimensional flow with the Womersley flow in the case where we used the negative of the axial dynamic pressure gradient  $p + \frac{1}{2}\rho u^2$  and the case where we used the negative of the axial static pressure gradient  $p$ . Although the match is excellent in both cases, the results show that we do get slightly better matching from using the dynamic pressure. This can be seen from Figs. 1 and 2.

To integrate the 1D theory with the Womersley theory we apply an iterative algorithm that allows us to feed information at the end of every cardiac cycle from the 1D theory to the Womersley theory and from the Womersley theory to the 1D theory. At every cardiac cycle iteration, the 1D equations of blood flow are solved. The solution gives us the pressure and velocity as a function of position along each artery, from which we can compute the dynamic pressure gradient. This pressure gradient is then used to drive the Womersley flow from which we can calculate the friction at the wall at each corresponding position along each artery and also correct the nonlinear terms based on the velocity profile information. In the next iteration of the cardiac cycle, the 1D equations of blood flow are solved again but with the right hand side adjusted by using the friction term of the previous iteration and the nonlinear terms corrected according to the velocity profile information from the previous iteration. At iteration zero, the friction is initialized to zero and the velocity profile is taken to be flat. At iteration  $n$ , the following system of equations is solved:

**Fig. 1** Matching of the one-dimensional flow with Womersley flow when Womersley model is driven by dynamic pressure gradient

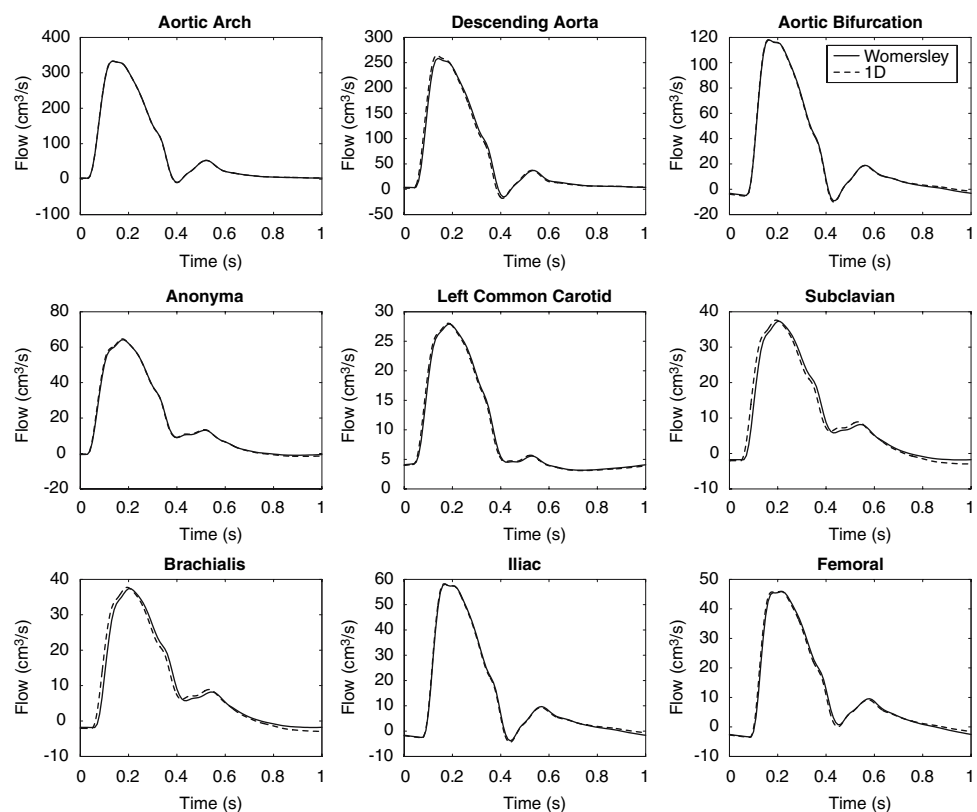
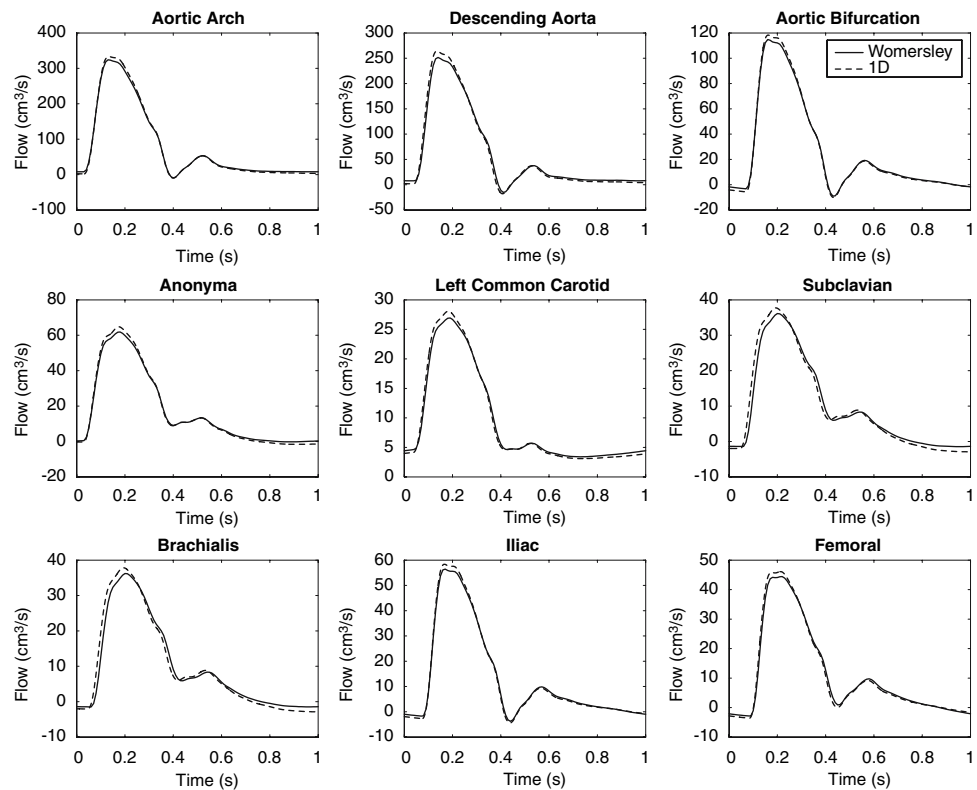


**Fig. 2** Matching of the one-dimensional flow with Womersley flow when Womersley model is driven by static pressure gradient



$$\frac{\partial}{\partial t} \begin{pmatrix} u_n \\ A_n \end{pmatrix} + \frac{\partial}{\partial x} \begin{pmatrix} -\frac{1}{2}u_n^2 + w_{n-1} + \frac{p(A_n)}{\rho} \\ u_n A_n \end{pmatrix} = \begin{pmatrix} \frac{(u_{n-1}^2 - w_{n-1})}{A_{n-1}} \frac{\partial A_{n-1}}{\partial x} + f_{n-1} \\ 0 \end{pmatrix} \quad (37)$$

### Characteristics and Riemann Invariants

To determine the number of boundary conditions needed at each of the different types of boundaries and junctions that arise in the arterial tree, and to solve for the velocity and cross-sectional area at boundary and junction points, we consider the characteristic equations and the integral form for the Riemann invariants (which actually vary in our case, see below) along those characteristics (Chorin et al. 1998; Courant et al. 1999). In the neighborhood of any boundary or junction points, we assume flat velocity profiles for simplicity. The two characteristic directions are:

$$\frac{dx}{dt} = u \pm \sqrt{\frac{Ap'(A)}{\rho}} \quad (38)$$

and the characteristic speeds are

$$u \pm \sqrt{\frac{Ap'(A)}{\rho}} \quad (39)$$

The propagation velocity  $\sqrt{\frac{Ap'(A)}{\rho}}$  is typically much larger than the blood velocity  $u$ , and hence we expect to have two characteristic directions. We will call the set of characteristics where the characteristic speed is given by  $u + \sqrt{\frac{Ap'(A)}{\rho}}$  the set of plus characteristics  $C+$ , and the other set the set of minus characteristics  $C-$ .

The Riemann invariants are given by the equations

$$\frac{d}{dt} \left( u \pm \int_{A_0}^A \sqrt{\frac{p'(A')\rho A'}{d}} A' - \int_{t_0}^t \frac{f}{\rho} dt' \right) = 0 \quad (40)$$

where the time derivative is that seen by an observer who moves along the  $C\pm$  characteristic. If we let

$$F(A) = \int_{A_0}^A \sqrt{\frac{p'(A')\rho A'}{d}} A' \quad (41)$$

then

$$\frac{d}{dt} \left( u \pm F(A) - \int_{t_0}^t \frac{f}{\rho} dt' \right) = 0 \quad (42)$$

The Riemann invariants by definition are  $u + F(A)$  on a  $C+$  characteristic and  $u - F(A)$  on a  $C-$  characteristic. As equation 42 shows, these quantities are invariant (each on its own type of characteristic) in the absence of friction. When friction is present, they vary in a manner that can be

computed from equation 42. This will be useful in the formulation of boundary conditions for our numerical scheme. The number of boundary conditions needed at a boundary or junction point of the arterial tree can be ascertained by counting the number of characteristics that arrive at that point from the interior of some arterial segment as one follows the characteristics *forward* in time. For example, at the heart ( $x = 0$ ), only the C– characteristic is arriving, and it brings with it one equation associated with its Riemann invariant. Since there are two unknowns ( $u$ ,  $A$ ), one boundary condition is needed. Similarly, at the distal end of any terminal arterial segment (i.e., at a “leaf” of the arterial tree) only the C+ characteristic is arriving, and again one boundary condition is needed. At a junction where the three arterial segments meet (the parent vessel and the two daughter vessels), three characteristics (C+ from the parent vessel and C– from each of the daughter vessels) are arriving, but there are 6 unknowns at any such junction ( $u$ ,  $A$ , in each of the three vessels) and therefore three boundary conditions are needed. The specific boundary conditions used in each case will be described in the next section.

### Boundary Conditions

There are three types of boundary conditions. The inflow boundary condition at the heart takes the form

$$uA|_{x=0} = Q_0(t) \quad (43)$$

where  $Q_0(t)$  is the cardiac output (volume per unit time) as a function of time. This is a periodic function, with the period of one cardiac cycle. It takes a shorter amount of time to get to the maximum from zero than to decrease from the maximum to zero. The area under the curve over one period is the stroke volume. An example of the cardiac output as a function of time over one cardiac cycle is shown in Fig. 3.

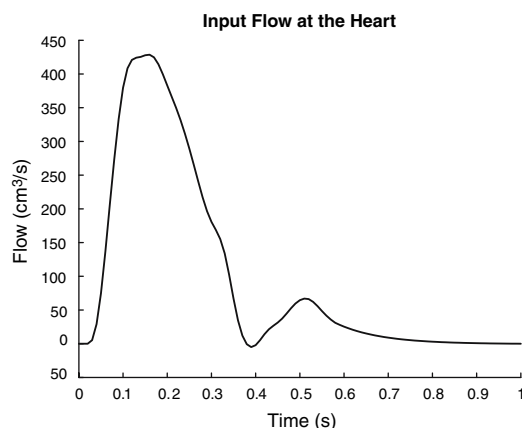


Fig. 3 Input flow at the heart used in the simulation

The second type of boundary condition is the outflow boundary condition at the extremity of a terminal branch of the model large-arterial tree. Large arteries are those in which viscous effects are small. We have compared two different formulations of this boundary condition. The first is a constant resistance model:

$$p = (uA)R \quad (44)$$

where  $R$  is called the *hemodynamic resistance*. This condition corresponds to an instantaneous response of the flow to the pressure, and therefore does not incorporate the possibly complicated dynamics of the small arteries that lie beyond the point where we (somewhat arbitrarily) decide to terminate the model. The pressure and the flow are forced to be synchronized. The other type of outflow boundary condition is based on a structured tree approach (Olufsen et al. 2000), in which the small arteries are assumed to have a recursive structure as defined below. Within a structured tree we linearize the Navier-Stokes (NS) equations, based on the assumption that flow in the smaller arteries is dominated by viscosity:

$$\begin{aligned} \rho \frac{\partial u}{\partial t} + \frac{\partial p}{\partial x} &= -\gamma u \\ C \frac{\partial p}{\partial t} + A_0 \frac{\partial u}{\partial x} &= 0 \end{aligned} \quad (45)$$

where  $\gamma = 8 \frac{\mu \pi}{A_0}$ ,  $u$  is the average velocity,  $A_0$  is the cross-sectional area of the vessel and  $C$  is called the *area compliance*. The friction term  $-\gamma \mu$  was calculated assuming Poiseuille flow i.e., a parabolic velocity profile. Let  $u(x,t) = U(x) e^{i\omega t}$  and  $p(x,t) = P(x) e^{i\omega t}$  (Later we take the real part so that the velocity and pressure are real). Substituting into equation 45 we get the following:

$$\begin{aligned} (\gamma + i\omega\rho)U(x) + \frac{dP(x)}{dx} &= 0 \\ i\omega CP(x) + A_0 \frac{dU(x)}{dx} &= 0 \end{aligned} \quad (46)$$

Solving this pair of equations for  $U(x)$ ,  $P(x)$  over an interval  $0 < x < L$ , where  $L$  is the length of the vessel, allows us to relate the values of these unknowns at  $x = 0$  to their values at  $x = L$ . We express this relationship in terms of the flow  $Q = UA_0$  instead of the velocity  $U$ . It then takes the form:

$$\begin{aligned} Q(0) &= \cosh(\lambda L)Q(L) + \frac{i\omega C}{\lambda} \sinh(\lambda L)P(L) \\ P(0) &= \frac{\lambda}{i\omega C} \sinh(\lambda L)Q(L) + \cosh(\lambda L)P(L) \end{aligned} \quad (47)$$

where  $\lambda = \sqrt{\frac{i\omega C(\gamma + i\omega\rho)}{A_0}}$ . If we let  $Q(L) = Y_L P(L)$ , where  $Y_L$  is called the *output admittance*, then we get the following expression for the *input admittance* in terms of  $Y_L$ :

$$Y_0(\omega) = \frac{Q(0)}{P(0)} = \frac{\cosh(\lambda L) * Y_L(\omega) + \frac{i\omega C}{\lambda} \sinh(\lambda L)}{\frac{\lambda}{i\omega C} \sinh(\lambda L)Y_L(\omega) + \cosh(\lambda L)} \quad (48)$$



Note that  $Y_0$  and  $Y_L$  are functions of  $\omega$ . If we then have a tree of small arteries, we can calculate the admittance at the root of the tree for each frequency  $\omega$ , given the admittance at the leaves of the tree by recursively applying equation 48. At a junction, we assume that there is no leakage and that therefore flow is conserved. We also assume that pressure is continuous across a junction. It therefore follows that admittances add, so that the admittance of a parent vessel is equal to the sum of admittances of its two daughter vessels. The terminal resistance at the leaves of the structured tree is set to zero, since we assume that the main source of resistance is the structured tree itself, and not the capillary bed that lies beyond the structured arterial tree. We assume that pressure and flow are periodic and therefore can be written as Fourier series. In the frequency domain, the boundary condition to be applied at the root of the structured tree is

$$P(\omega) = Q(\omega)Z(\omega) \quad (49)$$

where  $Z(\omega) = \frac{1}{Y(\omega)}$  is the input impedance of the whole structured tree at frequency  $\omega$ . This can be transformed back, using the convolution theorem, to the time domain, to give

$$p(x, t) = \frac{1}{T} \int_0^T Q(t - t')z(t')dt' \quad (50)$$

where  $z(t)$  is the inverse Fourier transform of  $Z(\omega)$ . Suppose that pressure and area are related by the state equation,  $p(A) = \frac{1}{2}\rho c^2 \left( \left( \frac{A}{A_0} \right)^2 - 1 \right)$  (which will be described in a later section), that flow  $Q = uA$ , and that velocity and area are related by the Riemann equation  $u = k - \frac{c}{A_0}(A - A_0)$ , where  $k$  is a constant. Substituting these expressions in 51, discretizing the resulting convolution integral and simplifying we get

$$(A^n)^2 \left( \frac{1}{2} \frac{\rho c^2}{A_0^2} + \frac{\Delta t}{T} \frac{c}{A_0} z(0) \right) - \Delta t z(0) A^n (-k^n - c) - \frac{1}{2} \rho c^2 - \frac{\Delta t}{T} \sum_{j=1}^{N-1} \left( k^{<n-j>_N} - \frac{c}{A_0} (A^{<n-j>_N} - A_0) \right) A^{<n-j>_N} z^j = 0 \quad (51)$$

This is a quadratic equation that can be solved for  $A^n$ , where  $A^n = A(L, N\Delta t)$ .  $L$  is the length of the artery,  $N\Delta t = T$  is the period of the cardiac cycle and  $< \cdot >_N$  denotes an operation modulo  $N$ . The structured tree boundary condition is a dynamic boundary condition that models the wave propagation effects of the pressure pulse, and is a more physiologically accurate model of the small arteries.

The junction boundary condition at the bifurcation point where one artery splits off into two arteries is the third type of boundary condition. Let the subscript 0 denote the

parent artery and denote the children arteries by the subscripts 1 and 2. At the bifurcation point, we are assuming that there is no leakage so the flow is conserved:

$$u_0 A_0 = u_1 A_1 + u_2 A_2 \quad (52)$$

We also assume that the pressure is continuous at the junction:

$$p_0 = p_1 = p_2 \quad (53)$$

Another boundary condition that one might possibly use in place of 54 is the Bernoulli condition, which is the conservation of static pressure  $p$  plus dynamic pressures  $\frac{1}{2}\rho u^2$ . However, we argue that 54 is the more appropriate one. It is known that at an artery bifurcation, the total cross-sectional area increases downstream, so that  $A_1 + A_2 \geq A_0$ . This means that we have a scenario similar to the one depicted in Fig. 4 at an artery bifurcation. In the ideal case where no vortices are formed, the Bernoulli relation  $p + \frac{1}{2}\rho u^2$  would hold along streamlines. However, since energy is spent to create the vortices in the corners, as shown in Fig. 4, the equation  $p_0 = p_1 = p_2$  is much more suitable for the case of arteries. The Bernoulli relation would be a suitable boundary condition if we were modeling veins since the flow would be the other way and energy will not be spent to create vortices. Note too that the quantity  $\frac{1}{2}\rho u^2$  is typically much smaller than the static pressure  $p$ , so in practice it makes little difference which of the two conditions we use. This is only true for arteries and not for veins, where  $p$  is much lower and the velocities, although somewhat lower, cannot be too much lower than in arteries. Therefore the question of which boundary condition to use is probably a more pressing one in the case of veins.

At the inflow and outflow boundary conditions, we have one equation and two unknown variables. Therefore in both cases, we need to derive one extra equation to be used for solving for the velocity and cross-sectional area at the respective boundary points. We do that by taking advantage of information along characteristics and get another equation the following way.

For the inflow condition at the heart, we calculate the fraction  $\gamma$  such that the C- characteristic leaving  $\gamma \Delta x$  from the ascending aorta at time  $t$  will hit the  $t$ -axis at  $t + \Delta t$ . We

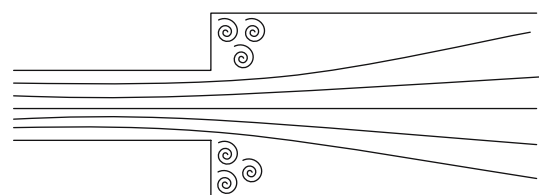


**Fig. 4** Separation of flow and vortex formation at the entrance region of a bifurcation

interpolate to find the values of  $u$  and  $A$  at  $\gamma \Delta x$ , which we then use to compute the constant  $k$  in the Riemann equation  $u + G(A) - \int_{t_0}^t \frac{f}{\rho} dt' = k$ . This gives us another equation for  $u$  and  $A$  at the point  $\Delta t$  which we can use with  $uA|_{x=0} = Q_0(t)$  to solve for  $u$  and  $A$  at the inflow boundary.

In a constant resistance model for the outflow boundary condition, pressure and flow ( $uA$ ) are related by 45. For the outflow boundary condition at the end of a terminal large artery vessel using a constant resistance model, we calculate the fraction  $\gamma$  such that the C+ characteristic leaving  $L - \gamma \Delta x$ , where  $L$  is the length of the vessel, from that terminal branch will hit the  $t$ -axis at  $t = \Delta t$ . We interpolate to find the values of  $u$  and  $A$  at  $\gamma \Delta x$ , which we then use to compute the constant  $k$  in the Riemann equation  $u - F(A) - \int_{t_0}^t \frac{f}{\rho} dt' = k$ . This gives us another equation for  $u$  and  $A$  at the point  $(0, t + \Delta t)$  which we can use with  $p = (uA) R$  to solve for  $u$  and  $A$  at end of each large artery terminal vessel.

For the bifurcation boundary condition, we calculate the fraction  $\gamma$  such that the C+ characteristic leaving  $\gamma \Delta x$  from the parent artery will hit the  $t$ -axis at  $t = \Delta t$ . We calculate similar fractions for the two daughter branches such that the C- characteristic leaving each of the daughter branches will hit the  $t$ -axis at  $t = \Delta t$ , see Fig. 5. We interpolate to find the values of  $u$  and  $A$  at  $\gamma \Delta x$  at the parent branch and similarly for the two daughter branches, which we then use to compute the constant  $k$  in the Riemann equation  $u - F(A) - \int_{t_0}^t \frac{f}{\rho} dt' = k$  for the parent branch and similarly  $u + F(A) - \int_{t_0}^t \frac{f}{\rho} dt' = k_{2,3}$  for each of the daughter branches. This gives us three equations for  $u_1, A_1, u_2, A_2, u_3$  and  $A_3$  at the point  $\Delta t$  which we can use with  $u_1 A_1 = u_2 A_2 + u_3 A_3$  and  $p_1 = p_2 = p_3$  to solve for all six unknowns at the bifurcation.

## Numerical Solver

In order to solve the system of Eq. 18 numerically, we expanded the term on the right-hand side of the momentum

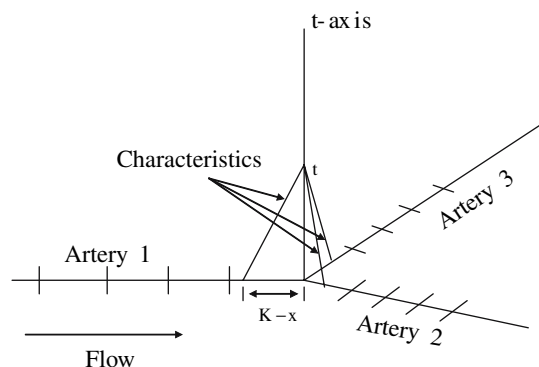


**Fig. 5** Plus and minus characteristics at the point of intersection in a bifurcation

equation,  $\frac{1}{A} \frac{\partial(A(u^2 - w))}{\partial x} = \frac{\partial}{\partial x} (u^2 - w) + \frac{u^2 - w}{A} \frac{\partial A}{\partial x}$  and moved over the term  $\frac{\partial}{\partial x} (u^2 - w)$  back into the nonlinear term on the left-hand side to give  $\frac{\partial}{\partial x} \left( -\frac{1}{2} u^2 + w + \frac{p(A)}{\rho} \right)$ . Note that  $w$  in this term depends on a complete cardiac cycle since it is a function of the velocity profile, which comes from the Womersley model, and which in turn requires the pressure gradient from one cardiac cycle. This  $w$  is therefore treated as a forcing term that is only updated once per cardiac cycle. Nevertheless, its contribution is maintained in the nonlinear part of the momentum equation, which is where it belongs.

The solver we use for this system of equations is the implementation of the two-step Richtmeyer Lax-Wendroff scheme (Richtmeyer et al. 1967 (Fig. 6):

Consider the hyperbolic system of equations

$$\frac{\partial g}{\partial t} + \frac{\partial G(g)}{\partial x} = H \quad (54)$$

where

$$\begin{aligned} g &= \begin{pmatrix} A \\ u \end{pmatrix} \\ G(g) &= \begin{pmatrix} uA \\ -\frac{1}{2} u^2 + w + \frac{p(A)}{\rho} \end{pmatrix} = \begin{pmatrix} \phi \\ \psi \end{pmatrix} \\ H &= \begin{pmatrix} h_1 \\ h_2 \end{pmatrix} = \begin{pmatrix} 0 \\ \frac{u^2 - w}{A} \frac{\partial A}{\partial x} + f \end{pmatrix} \end{aligned} \quad (55)$$

Then the scheme is as follows, for interior points of the mesh:

$$\begin{aligned} A_{l+\frac{1}{2}}^{n+\frac{1}{2}} &= \frac{1}{2} (A_l^n + A_{l+1}^n) - \frac{\Delta t}{2\Delta x} (\phi_{l+1}^n - \phi_l^n) \\ &\quad + \frac{\Delta t}{4} ((h_1)_{l+1}^n - (h_1)_l^n) \end{aligned} \quad (56)$$

$$u_{l+\frac{1}{2}}^{n+\frac{1}{2}} = \frac{1}{2} (u_l^n + u_{l+1}^n) - \frac{\Delta t}{\Delta x} (\psi_{l+1}^n - \psi_l^n) + \frac{\Delta t}{4} ((h_2)_{l+1}^n - (h_2)_l^n) \quad (57)$$

$$A_l^{n+1} = A_l^n - \frac{\Delta t}{\Delta x} (\phi_{l+\frac{1}{2}}^{n+\frac{1}{2}} - \phi_{l-\frac{1}{2}}^{n+\frac{1}{2}}) + \frac{\Delta t}{2} ((h_1)_{l+\frac{1}{2}}^{n+\frac{1}{2}} - (h_1)_{l-\frac{1}{2}}^{n+\frac{1}{2}}) \quad (58)$$

$$u_l^{n+1} = u_l^n - \frac{\Delta t}{\Delta x} (\psi_{l+\frac{1}{2}}^{n+\frac{1}{2}} - \psi_{l-\frac{1}{2}}^{n+\frac{1}{2}}) + \frac{\Delta t}{2} ((h_2)_{l+\frac{1}{2}}^{n+\frac{1}{2}} - (h_2)_{l-\frac{1}{2}}^{n+\frac{1}{2}}) \quad (59)$$

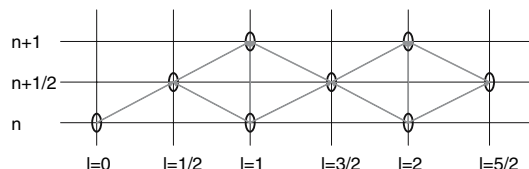


**Fig. 6** Stencil of the two-step Richtmeyer version of the Lax-Wendroff method

By doing some analysis on the 1D model 19, where the right-hand side is taken to be zero, one can derive a condition, known as the Courant-Friedrichs-Lewy (CFL) condition, which is a necessary condition for the stability of the Lax-Wendroff scheme. First we find the eigenvalues of the matrix  $B = \begin{pmatrix} u & A \\ \frac{p'(A)}{\rho} & u \end{pmatrix}$ . The eigenvalues are  $\lambda = u \pm \sqrt{A \frac{p'(A)}{\rho}}$ . Next we proceed to find the eigenvectors of the matrix  $B^T$  and get  $w = \begin{pmatrix} \pm \sqrt{\frac{p'(A)}{\rho}} \\ 1 \end{pmatrix}$ . We then try and put  $w$  in the form  $w = \begin{pmatrix} \frac{\partial \Gamma}{\partial A} \\ \frac{\partial \Gamma}{\partial u} \end{pmatrix}$ , i.e. find  $\Gamma = \Gamma(u, A)$ , such that  $\frac{\partial \Gamma}{\partial A} = w_1$  and  $\frac{\partial \Gamma}{\partial u} = w_2$ , where  $w = \begin{pmatrix} w_1 \\ w_2 \end{pmatrix}$ . Finding such a function  $\Gamma$  is possible since  $\frac{\partial w_1}{\partial u} = \frac{\partial w_2}{\partial A} = 0$ . By integration, we find that  $\Gamma^\pm = u \pm \int^A \sqrt{\frac{p'(\tilde{A})}{A\rho}} d\tilde{A}$ . Comparing the expressions for  $\lambda$  and  $\Gamma$  to the expressions in 40 and 43 respectively, we find that  $\lambda$  represents the characteristic speeds and  $\Gamma$  represents the Riemann invariants along the characteristics (in the absence of a friction force). Let  $c = \sqrt{A \frac{p'(A)}{\rho}}$  denote the wave speed. Given an arbitrary point in the  $(x, t)$  plane, the domain of dependence of this point is the region bounded by the plus and minus characteristics  $C+$  and  $C-$  going through the point, and the  $x$ -axis. The numerical domain of dependence of a point  $(x, t)$  must contain its actual domain of dependence. If not, consider initial data which are nonzero only on the part of the actual domain of dependence which lies outside of the numerical domain of dependence of the point  $(x, t)$ . Then the computed solution at  $(x, t)$  will necessarily be zero for all choices of  $\Delta x, \Delta t$  consistent with the specified numerical domain of dependence (since the initial data are zero within the numerical domain of dependence of  $(x, t)$ ), but the actual solution evaluated at  $(x, t)$  will be some nonzero value, so convergence is impossible, since a sequence of zeros cannot converge to a non-zero value. Since  $\frac{dx}{dt} = u \pm c$  along characteristics, this condition translates  $\frac{\Delta t}{\Delta x} \leq |u \pm c|^{-1}$ , which is the CFL condition (Courant et al. 1999).

## Convergence Results

Our numerical experiments show that the iterative algorithm we described to solve the system of Eq. 37 is overall a second order method for solving 1D blood flow equations, including friction, without any assumptions on the velocity profile. Moreover, the solution settles down after a certain number of cardiac iterations. To show the second order accuracy of our numerical algorithm, we set up a tree of three branches: a parent branch and two daughter branches. This setup tests all the components of the system. At the heart, we used a smooth initial condition, shown in Fig. 7, which is necessary to get second order convergence:

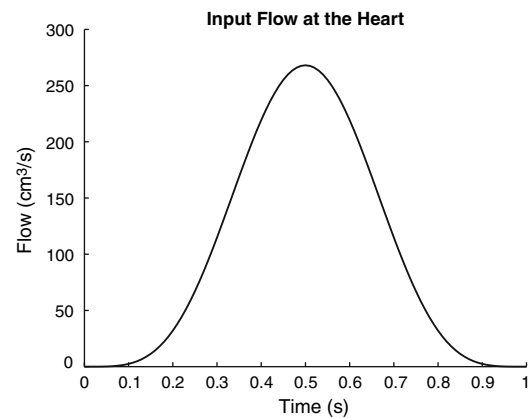


Fig. 7 Input flow at the heart used in the convergence study

Figures 8, 9, 10 and 11 show the convergence of the solution in the L2 norm, L1 norm and pointwise in the three arteries.

## Simulation Results

To validate the blood flow model, we use MRI data of a healthy male subject provided by Mette Olufsen (Olufsen et al. 2000). The data were recorded by E.M Pedersen and Y. Kim at Skejby University Hospital in Denmark. The arterial tree that we simulated is drawn in Fig. 12 and the geometric parameters of the model arterial tree are listed in Table 1.

The pressure-area relationship used for the large arteries was  $p - p_0 = \frac{1}{2} \rho c^2 \left( \left( \frac{A}{A_0} \right)^2 - 1 \right)$ , where  $c$  is the wave speed and  $A_0$  is the cross-sectional area when  $p = p_0$ . The compliance model used for the small arteries was the one used by Olufsen (Olufsen et al. 2000; Ottesen et al. 2004), namely  $C = \frac{3}{2} A_0 \frac{r_0}{Eh}$ , where  $\frac{Eh}{r_0} = k_1 e^{k_2 r_0} + k_3$ ,  $k_1 = 2.00 \times 10^7 \frac{g}{s^2 cm}$ ,  $k_2 = -22.53 \text{ cm}^{-1}$  and  $k_3 = 8.65 \times 10^5 \frac{g}{s^2 cm}$ .

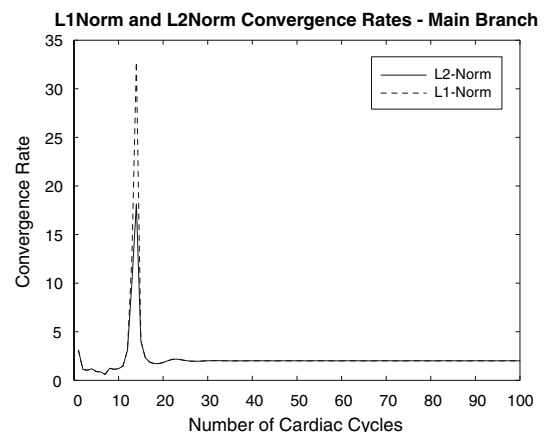
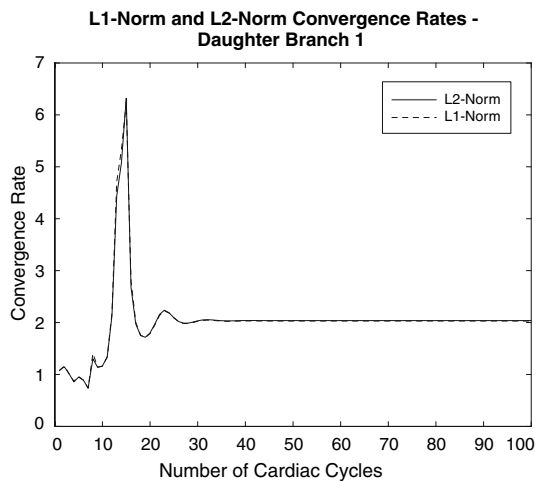
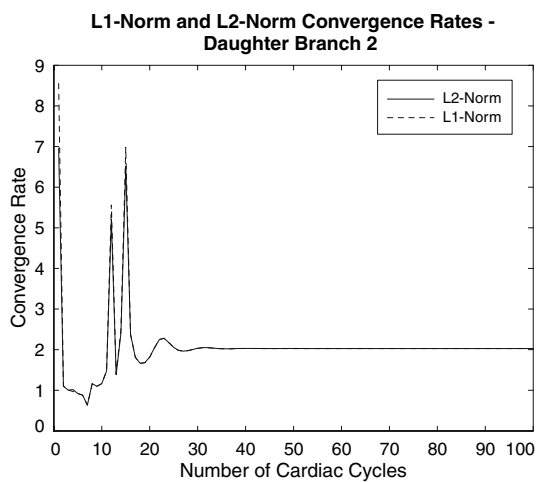


Fig. 8 L1 and L2 convergence in the main branch



**Fig. 9** L1 and L2 convergence in daughter branch 1



**Fig. 10** L1 and L2 convergence in daughter branch 2

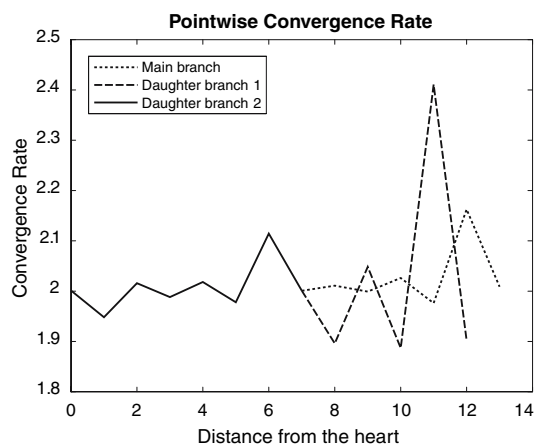


**Fig. 11** Pointwise convergence along the three-vessel tree used in the convergence study

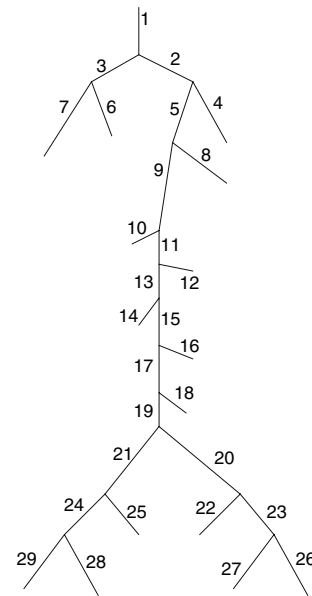


**Fig. 12** Illustration of the arterial tree simulated

(Stergiopoulos et al. 1992). For the small arteries, the structured tree approach requires three more parameters. One parameter,  $\xi$ , is used in the power law  $r_p^\xi = r_{d_1}^\xi + r_{d_2}^\xi$ , which dictates how the radius is changed across a bifurcation. Here the subscript  $p$  denotes the parent vessel, and the subscripts  $d_1$  and  $d_2$  denote the daughter vessels. The other parameter,  $\eta$ , is the area asymmetry ratio, given by  $\eta = \frac{r_{d_1}^2}{r_{d_2}^2}$  (Zamir 1999). The two parameters  $\xi$  and  $\eta$  were not chosen to be fixed but varied based on the radius of the vessel. Thus they vary even within a given structured tree. We have chosen  $\xi = 2.5$ ,  $\eta = 0.4$  for radius  $r > 250 \mu\text{m}$ ,  $\xi = 2.76$ ,  $\eta = 0.6$  for radius  $250 \mu\text{m} > r > 50 \mu\text{m}$ , and  $\xi = 2.99$ ,  $\eta = 0.9$  for radius  $r < 50 \mu\text{m}$  (Steele et al. 2003; Iberall 1967). The third parameter  $L_{tr}$ , is the ratio of the length of each artery to the radius (Iberall 1967). This parameter was chosen as a global constant, the same for all structured trees, and adjusted to get the correct steady-state impedance for the arterial tree as a whole. Note that, given  $r_p$ , the two equations  $r_p^\xi = r_{d_1}^\xi + r_{d_2}^\xi$  and  $\eta = \frac{r_{d_1}^2}{r_{d_2}^2}$  can be thought of as a pair of nonlinear equations for  $r_{d_1}$  and  $r_{d_2}$ . The solution of this nonlinear system determines the asymmetry at the bifurcation in question.

The first simulation shown in Figs. 13 and 14 show the effect of using Womersley theory both to compute the friction term and to correct the nonlinear terms with the Womersley velocity profiles. We expect the term  $\frac{\partial(A(u^2-w))}{\partial x}$  to be small under normal physiological conditions. This term has two components. One depends on the rate of change of the velocity profile from one location along the vessel to the other. The other depends on the change of cross-sectional area as a function of position,

**Table 1** This table contains the arterial tree dimensions used in the simulations

Artery number	Artery name	Length (cm)	Radius (cm)	$r_{\min}$ (cm)
1	Ascending aorta	7.0	1.195	–
2	Anonyma	3.5	0.700	–
3	Aortic arch 1	1.8	1.125	–
4	Left Common carotid	19.0	0.2850	0.03
5	Aortic arch 2	1.0	1.1	–
6	Subclavian	43.0	0.36	0.01
7	Right common carotid	17.0	0.2850	0.02
8	Brachial	43.0	0.36	0.01
9	Thoracic aorta	18.0	0.97	–
10	Celiac axis	3.0	0.3	0.02
11	Abdominal aorta 1	2.0	0.84	–
12	Superior mesentric	5.0	0.33	0.02
13	Abdominal aorta 2	2.0	0.815	–
14	Renal 1	3.0	0.265	0.02
15	Abdominal aorta 3	1.0	0.795	–
16	Renal 2	3.0	0.265	0.02
17	Abdominal aorta 4	6.0	0.760	–
18	Inferior mesentric	4.0	0.19	0.01
19	Abdominal aorta 5	3.0	0.715	–
20	External iliac left	6.5	0.44	–
21	External iliac right	6.5	0.44	–
22	Femoral left	13.0	0.415	–
23	Internal iliac left	4.5	0.20	0.01
24	Femoral right	13.0	0.415	–
25	Internal iliac right	4.5	0.20	0.01
26	Deep femoral left	11.0	0.20	0.01
27	Femoral left	44.0	0.35	0.01
28	Deep femoral right	11.0	0.20	0.01
29	Femoral right	44.0	0.35	0.01

The data in this table were provided by Mette Olufsen (Olufsen et al. 2000). The radius used for each vessel is the average of inlet radius and outlet radius for that vessel.  $r_{\min}$  is the radius of the smallest vessel in a given structured tree associated with a terminal branch. Topology of the arterial tree used is defined in Fig. 10

namely  $\frac{\partial A}{\partial x}$ . Since the characteristic wavelength in the arterial system is very large, there does not occur, under normal conditions, large changes in cross-sectional area  $A$  over a small distance, we expect the term  $\frac{\partial(A(u^2-w))}{\partial x}$  to be small. We therefore do not see a significant change in the larger arteries due to the adjustment of the nonlinear terms using the Womersley velocity profiles. However, the flows calculated using the friction computed from Womersley theory do show some change from those calculated using a simple friction model.

Combining the one-dimensional model with the Womersley model enables us to compute the shear stress at

the wall without assuming an a priori velocity profile. Moreover, it also allows us to compute the velocity profile at any location in the arterial system, at any given time. Figure 15 shows the velocity profile at nine different locations in the arterial tree. Each curve represents the velocity profile at a certain location at a specific time in the cardiac cycle. The velocity profiles show areas where boundary layer flow separation might be expected to occur, indicated by the reversal of flow near the boundary. Moreover, the velocity profiles display the wide range of Womersley number that occurs in the circulation, due to the varying shapes we see in the plots. Some of the velocity profiles show a Poiseuille-like profile indicating a very small Womersley number or quasi-steady flow. Others show more flat profiles, indicating higher Womersley number, or unsteady flow. We also see therefore that the assumptions of parabolic profile or flat profile with boundary layer near the wall often used to calculate the friction term are not correct assumptions.

We also compare the flow and pressure along the arterial tree using four different types of friction models, and using structured trees for the small arteries model. The four different types of friction models used were the Womersley model of this paper, a model with no friction, another where the velocity profile is assumed to be Poiseuillian, and the last with the velocity profile flat except for a boundary layer near the wall. The flow and pressure obtained using each of these models is plotted with the corresponding flow MRI data at nine different location in the arterial tree. In Figs. 16 and 17, we see that the flows and pressures are similar, regardless of which friction model is used. In the small differences that we do see, however, the flow and pressure waveforms obtained using the Womersley velocity profiles differ the most from the results obtained using the other models. The differences in the smaller blood vessels are primarily because of the different ways friction is modeled, since it is in the smaller arteries that friction plays an important role.

We have also considered the effect of changing the manner in which the small arteries are modeled on the flow and pressure in the large arteries. We compared a structured tree model with a pure resistance model for the small arteries. The flow and pressure resulting from using both models are plotted at nine different locations of the arterial tree, along with the corresponding flow MRI data. Figures 18 and 19 show that using structured trees we get much less reflection than using a pure resistance model for the small arteries. This is primarily because the dynamic response of the small arteries modeled by structured trees as opposed to the static response imposed by a pure resistance model. Using structured trees, moreover, we are able to see clearly the dicrotic wave (Feinberg and Lax 1958; Lax et al. 1956) in the pressure waveforms. The



**Fig. 13** Comparison of flow with and without Womersley profiles

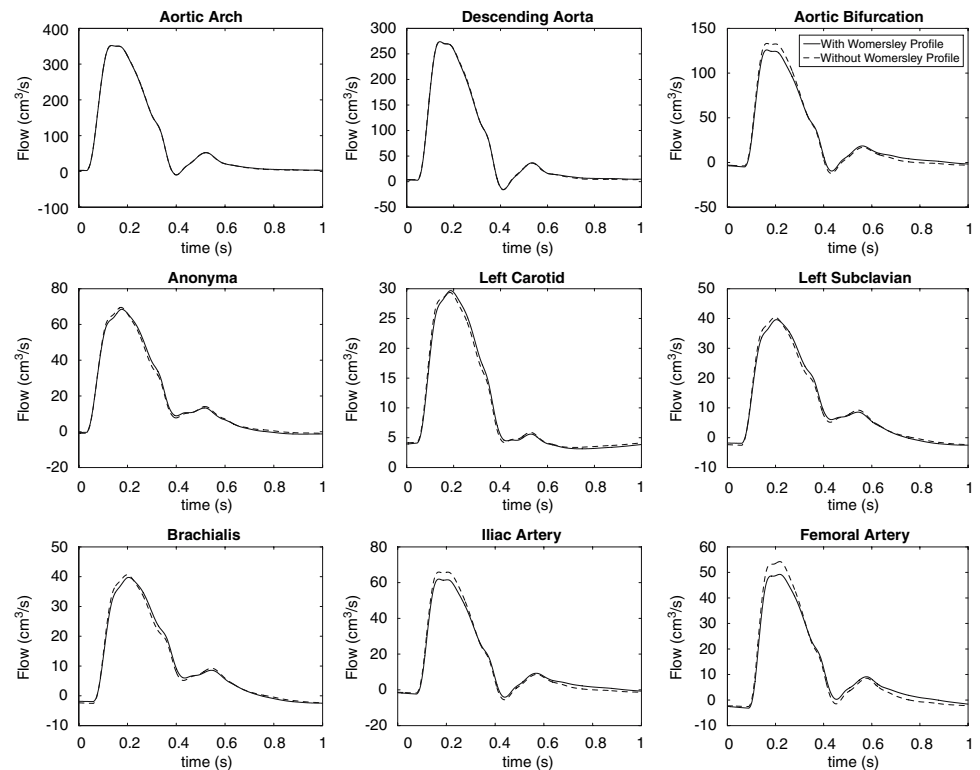
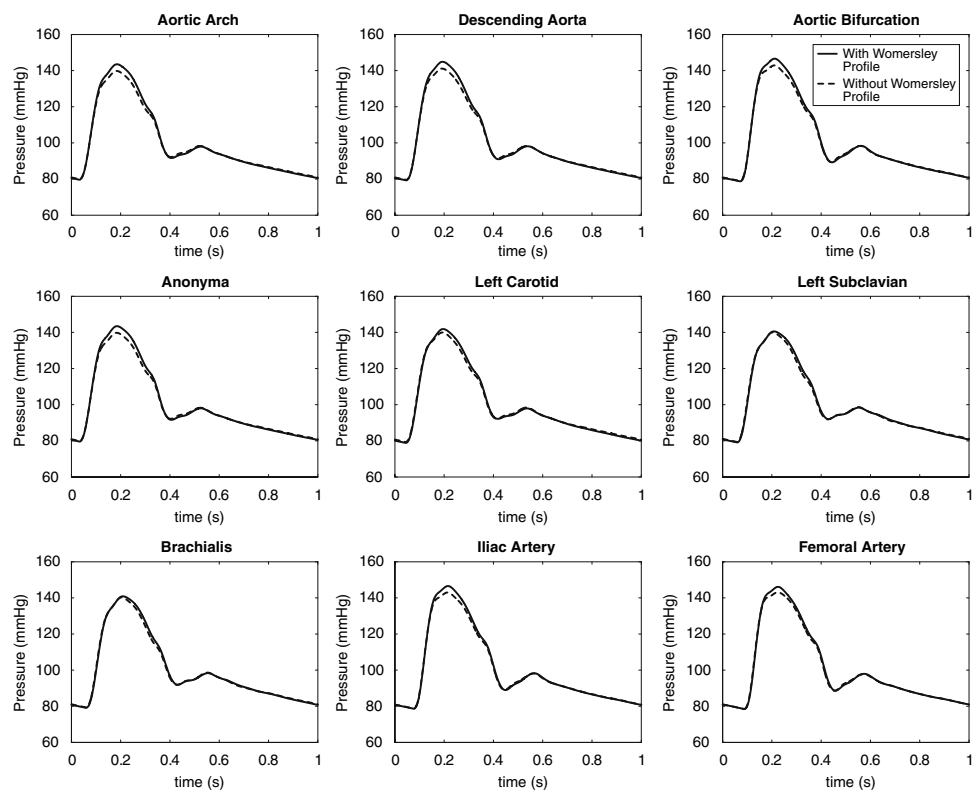


**Fig. 14** Comparison of pressure with and without Womersley profiles



pressure waveforms simulated using the pure resistance model do not have the dicrotic wave. Another important point is that the pressure pulse generated using the

structured tree model at each of the nine locations displayed in Fig. 19 is smaller than the one generated using the pure resistance model. This is because the structured

**Fig. 15** Velocity profiles at various locations in the arterial tree simulated using Womersley model combined with 1D model

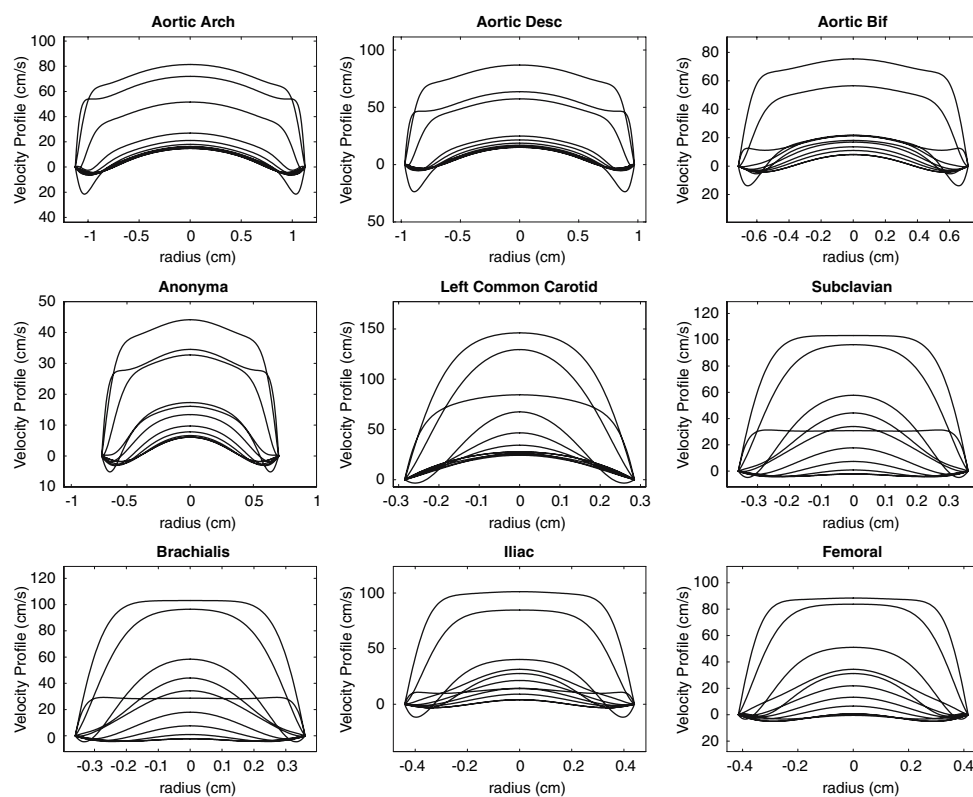
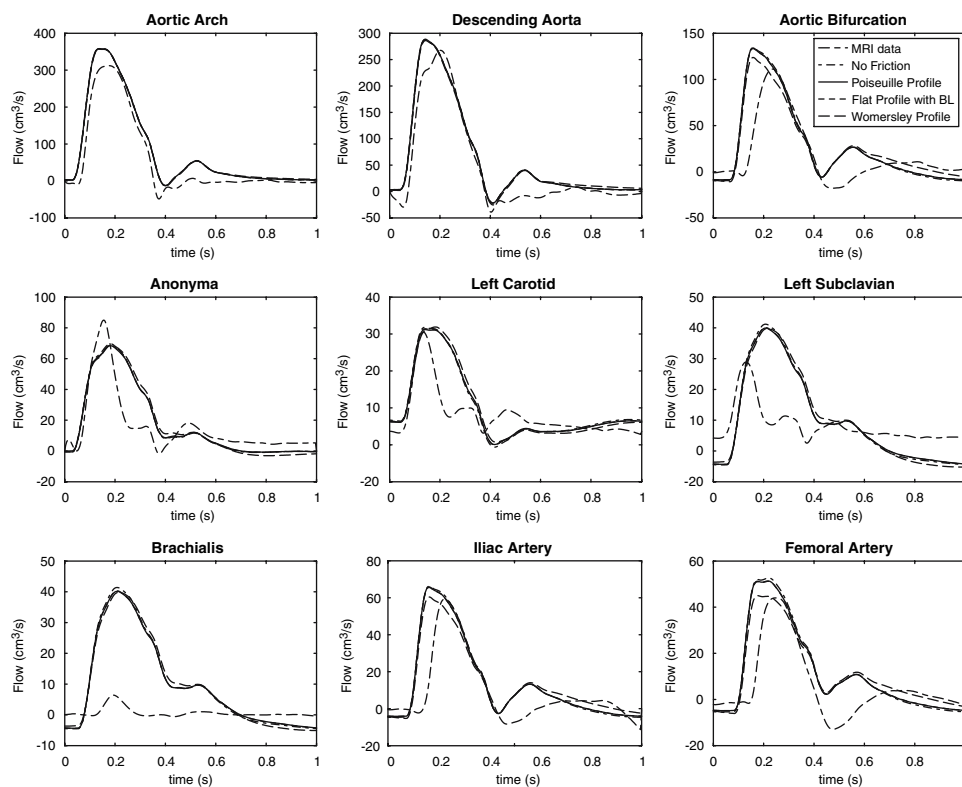


**Fig. 16** Comparison of flow waveforms simulated using different friction models



tree adds compliance to the arterial tree by including the compliance of the small arteries. The tree being more compliant results in a smaller pressure pulse. The pulse

generated by the structured tree is close to the actual pressure pulse of 120 mmHg over 80 mmHg of the subject on which the MRI was done.

**Fig. 17** Comparison of pressure waveforms simulated using different friction models

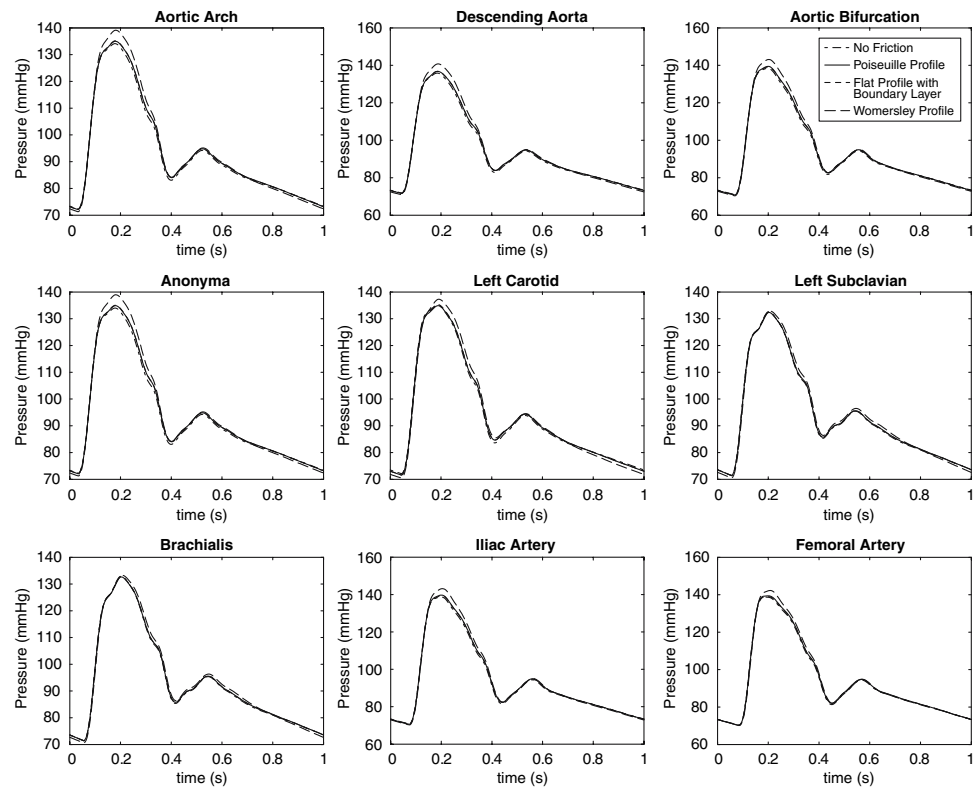
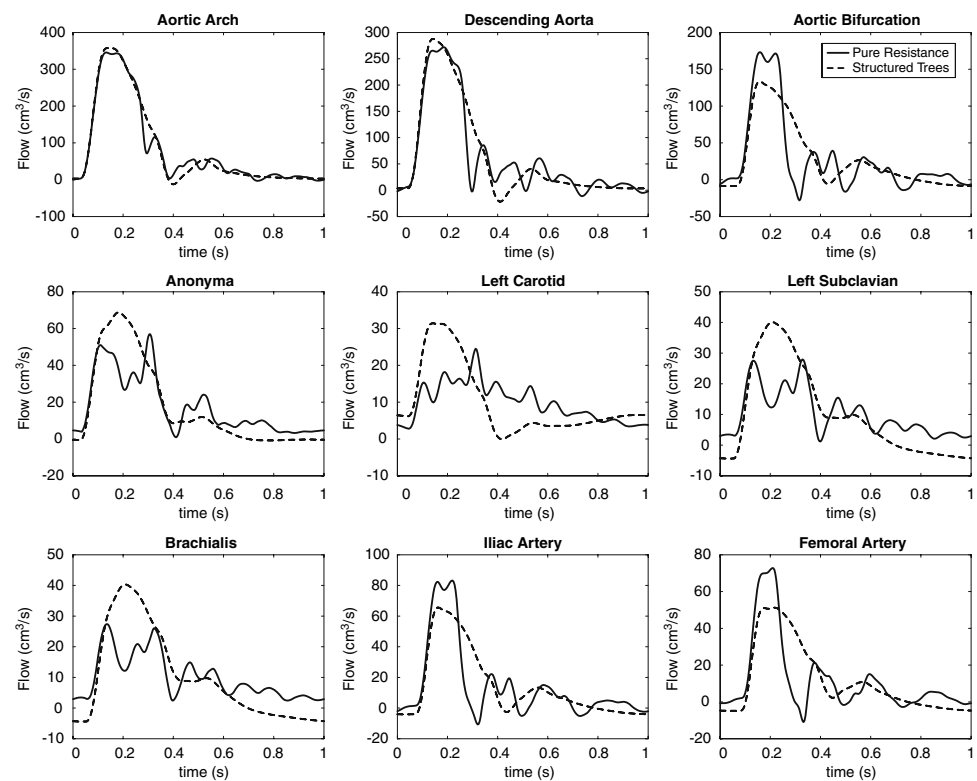


**Fig. 18** Comparison of flow waveforms simulated using two different models for the small arteries



There are three important physiological flow characteristics of the arterial pressure pulse (Nichols et al. 1998; Calfisch et al. 1980) that we can observe in our simulation

results, see Fig. 20. The systolic pressure increases with increasing distance downstream from the heart and the part of the pressure pulse from the foot to the peak becomes

**Fig. 19** Comparison of pressure waveforms simulated using two different models for the small arteries

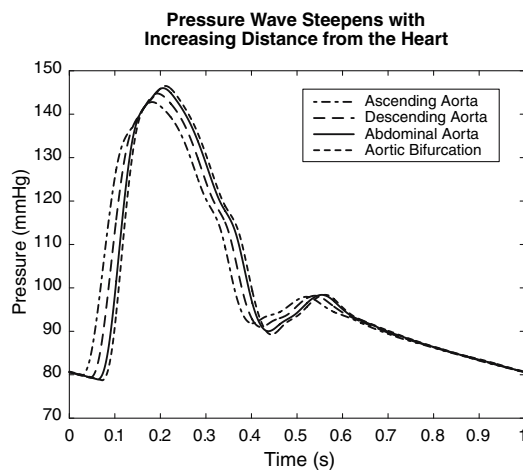
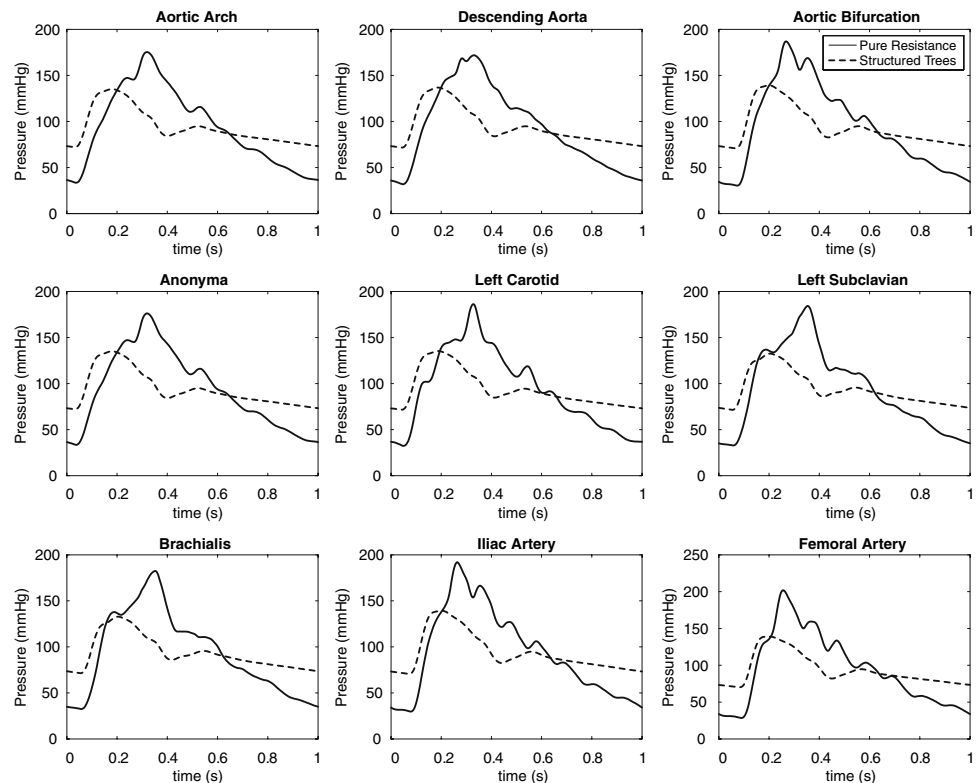


**Fig. 20** Steepening of the pressure waveform as distance from the heart increases

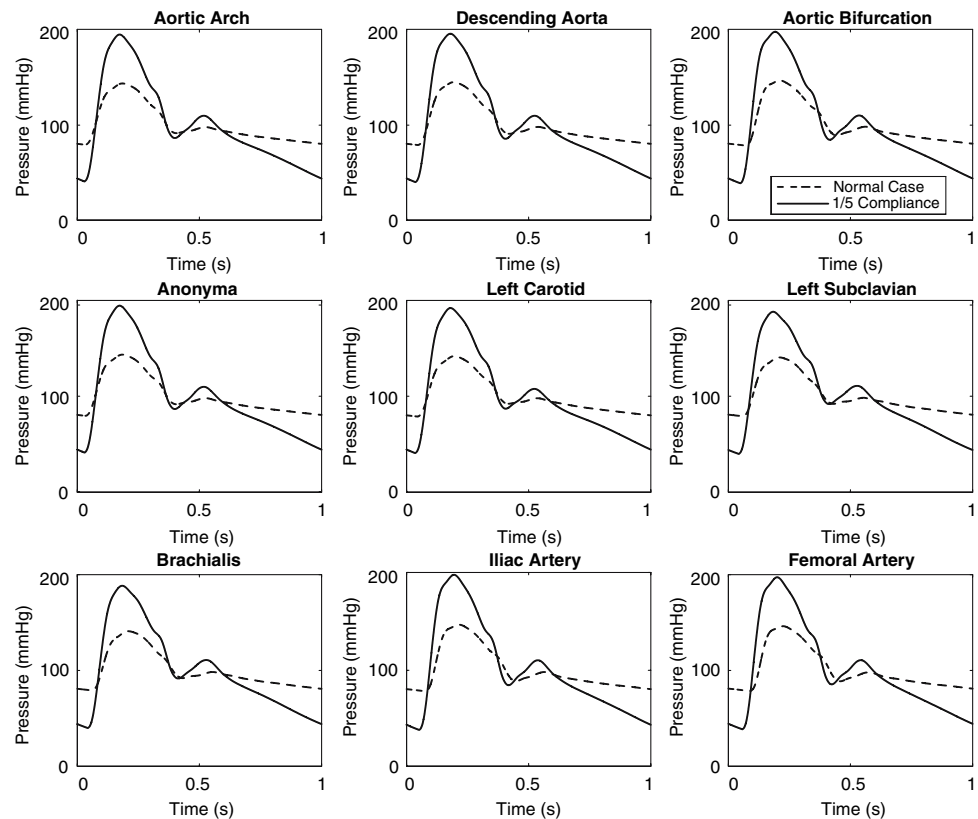
steeper. Moreover, the mean arterial pressure decreases slightly with increasing distance downstream of the heart because of the cumulative effect of friction on the propagation of the arterial pulse.

In hypertension, there are two competing theories on the initiation of the disease process (Coleman et al. 1971; Mendelsohn 2005). One theory is that there is an initial decrease in vascular compliance, which causes the systolic pressure to go up. Vascular smooth muscle cell abnormalities alter the contractile state of the cell. Changing the

set point of resting vascular tone initiates hypertension. The kidney is also known to have a set point for regulating the blood pressure. The other way in which it is thought that hypertension is initiated is starting in the kidney, and not with the vasculature. Within the kidney itself, complex processes cause the elevation of the blood pressure set point. The kidney then increases the fluid volume re-absorbed into the circulation, which in turn increases cardiac output, but also causes a change in compliance in the vasculature (Coleman et al. 1971). Following the increase of cardiac output, total peripheral resistance increases and cardiac output returns to approximately normal level. It is then the increase in total peripheral resistance that sustains the state of hypertension. However, if the set point of the kidney is not changed, it will regulate the blood volume in such a way as to bring the blood pressure to a normal value. In either scenario, the body responds to maintain the flow of blood through the circulation.

In an effort to model some aspects of the early stages of hypertension, we have simulated the effect of reduced compliance on pressure and flow waveforms under three different scenarios. We first changed the arterial compliance to be one-fifth of its value everywhere in the arterial tree (including the small vasculature) and looked for changes in the resulting pressure and flow waveforms. Figure 21 shows the changes in the pressure waveforms. The pulse pressure increased significantly. The systolic pressure increased and the diastolic pressure decreased.

**Fig. 21** Effect of decreased compliance on pressure waveform



Decreasing the compliance also increased the wave speed, which can be seen from the figures as a decrease in the delay of the pressure waveform to reach arteries downstream. However, the change in compliance has little effect on the flow. We then kept the compliance of the small vasculature fixed at its original value, and changed the compliance of the large arteries to one-fifth its original value. Figure 22 shows the resulting changes in the pressure waveforms. We see that the systolic pressure increased, though not as much as in the previous experiment. Moreover, we notice that the diastolic pressure drops only slightly. This is consistent with observations in the case of isolated systolic hypertension, as occurs for example in aging (Franklin 2004; Griffith et al. 2005; Nichols 2005). An increase in the wave speed is still evident from the decrease in the delay of the pressure waveforms to reach downstream arteries. The effect on the flow waveforms is consistently small. In the last experiment, we kept the compliance of the large arteries fixed at the original value and changed the compliance of the small vasculature to be one-fifth the original value. Figure 23 summarizes the changes to the pressure waveforms. In this case, the systolic pressure increases only slightly while the diastolic pressure dropped significantly. The diastolic pressure does not, however, drop as much as in the case in which the compliance of both the large and small arteries was

changed by the same amount. Moreover, we note that the diastolic wave in the pressure waveforms has diminished.

### Taylor Diffusion Combined with Blood Flow Simulation in a Vessel

In the previous section, we presented the simulation results for an arterial tree, with a one-dimensional model of blood flow in the large arteries, including a structured tree model of the small arteries. In this section, we use the simulated brachial artery velocity profiles to solve for the propagation of a concentration distribution by convection and diffusion through the artery. The calculation of the axial concentration profile of a solute transported by a time-independent flow in a rigid straight pipe was first addressed by Taylor (1953). Taylor showed that in the frame of reference moving with velocity  $\frac{u_0}{2}$ , the concentration of the solute satisfied the diffusion equation, with a diffusion coefficient of  $\frac{a^2 u_0^2}{192D}$ , where  $D$  is the coefficient of molecular diffusion for the solute and  $a$  is the radius of the pipe. A diffusion equation for the mean concentration profile along the axial-direction in a pipe in the case of time-dependent flow was derived in (Azer 2005, 2006) using asymptotic analysis. The convection-diffusion equation derived in (Azer 2005) and used here is given below:



**Fig. 22** Effect of changing the compliance of the large arteries on the pressure waveform

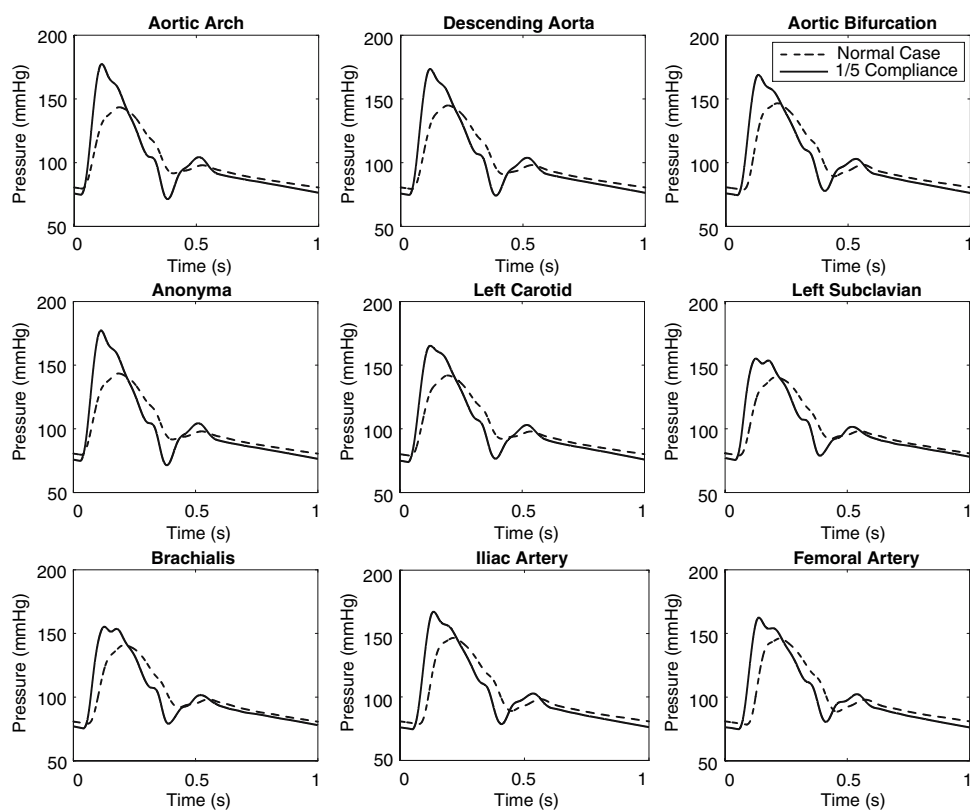
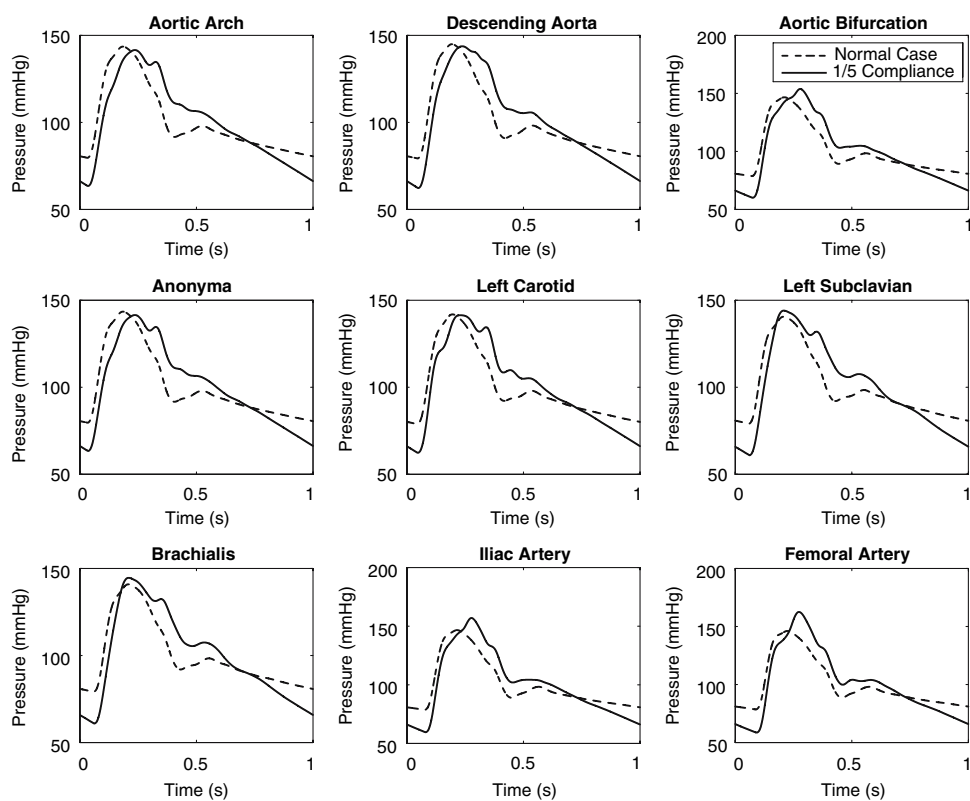


**Fig. 23** Effect of changing the compliance of the small vasculature on the pressure waveforms in the large arteries



$$\frac{\partial C}{\partial t} + \frac{\partial(x_0'(t; x)C)}{\partial x} = \frac{\partial}{\partial x} \left( D_{\text{eff}}(t; x) \frac{\partial C_0}{\partial x} \right) \quad (60)$$

where

$$\begin{aligned} D_{\text{eff}} = & \frac{2a^2}{D} \left( x_0'(t, u_0) \left( -\frac{1}{4} \int_0^1 (zf(z) + 2z \log(z) - z^3 f(z)) dz \right) \right. \\ & + \int_0^1 \frac{z^3}{4} x_0'(t, u_0) V(az, t; a) dz \\ & - \int_0^1 zf(z) \log(z) \int_0^z \zeta f(\zeta) d\zeta dz \\ & \left. - \int_0^1 zf(z) \int_0^z \zeta f(\zeta) \log(\zeta) d\zeta dz - \frac{1}{16} x_0'(t, u_0)^2 dz \right) + D \end{aligned} \quad (61)$$

and  $C$  is the concentration of solute,  $D$  is the coefficient of molecular diffusion of the solute,  $r$  is the radial variable,  $x$  is distance parallel to axis of the pipe,  $t$  is time,  $a$  is the radius of the pipe,  $V(r, t; a) = u_0(t) f(r, t; a)$  is the axial velocity of the moving fluid, where  $\frac{u_0(t)}{2}$  is the average velocity over a cross-section at a given time  $t$ ,  $x_0'$  is the average of the axial velocity over a cross-section of the pipe.

The numerical scheme used was provided by Jeff Saltzman (Saltzman 1994). A second order implicit method is used for the diffusion term. The convection term is discretized using a second order upwind method. The details of the numerical methods can be found in (Azer 2006).

The simulated flow, pressure and velocity profiles are shown in Figs. 24, 25 and 26. The velocity profiles are needed to compute the effective diffusion coefficient and the convection term. We ran the simulation with the molecular diffusion coefficient set to  $0.1 \text{ cm}^2/\text{s}$  and

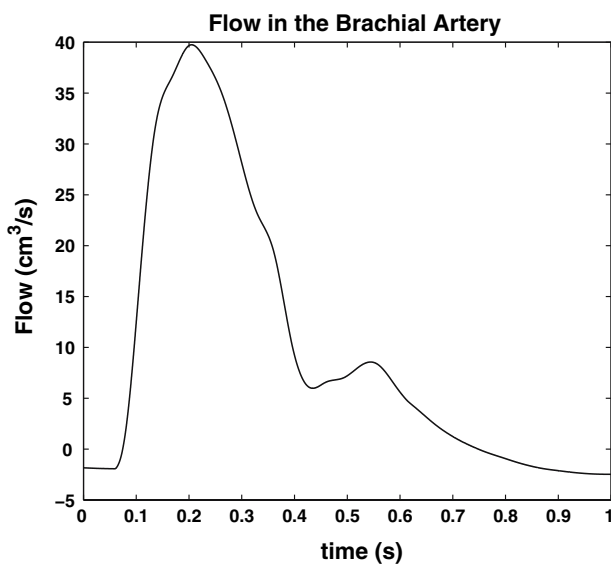


Fig. 24 Flow at a given  $x$ -location in the Brachial artery

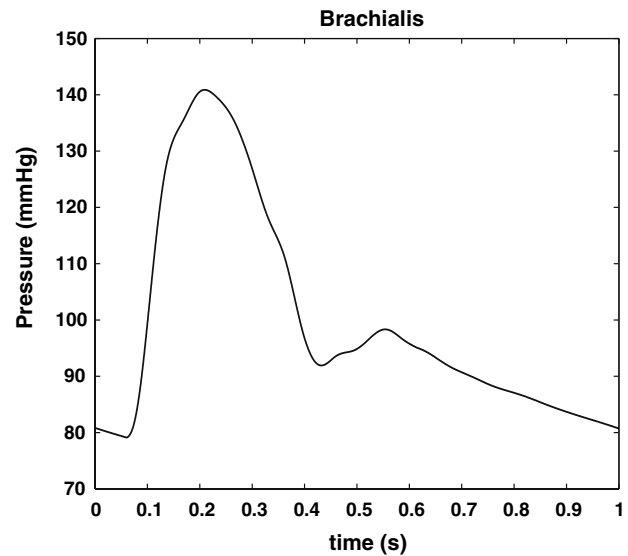


Fig. 25 Pressure at a given  $x$ -location in the Brachial artery

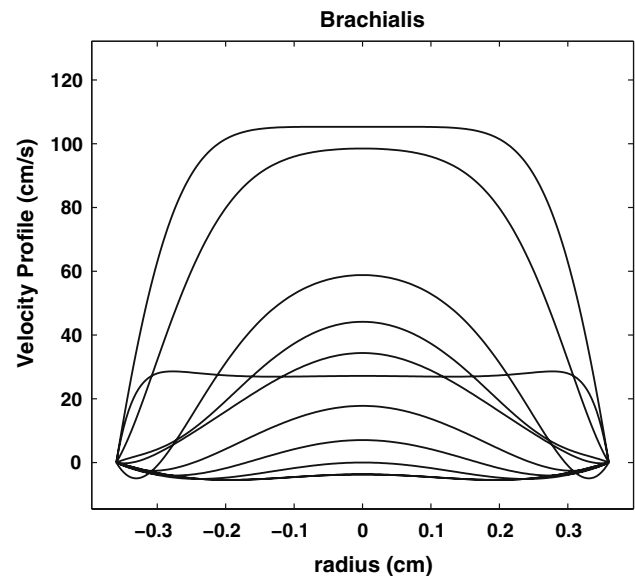
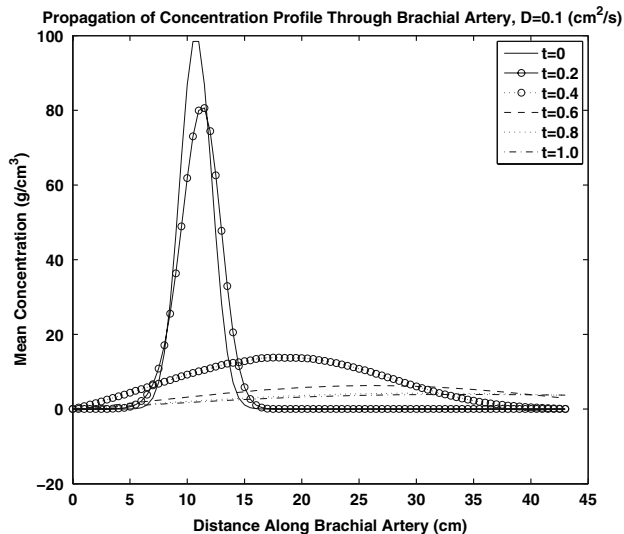
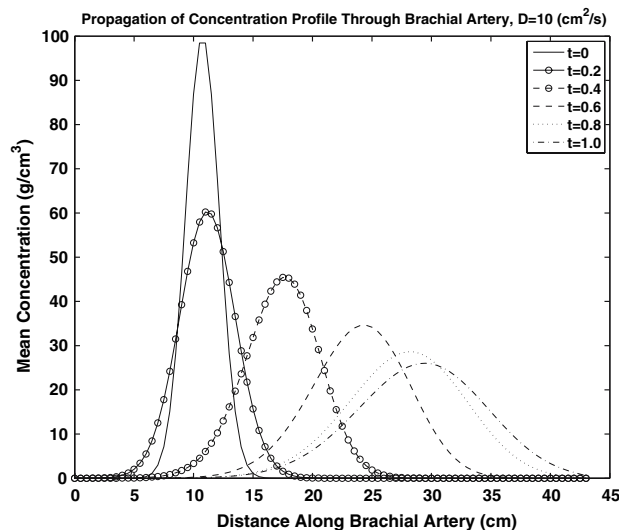


Fig. 26 Velocity profiles at a given  $x$ -location in the Brachial artery

$10 \text{ cm}^2/\text{s}$ . The concentration was recorded at five different time points during the cardiac cycle. The right boundary condition was a free boundary. Figures 27 and 28 show the concentrations when the molecular diffusion coefficient was set to  $0.1 \text{ cm}^2/\text{s}$  and  $10 \text{ cm}^2/\text{s}$ , respectively. We note that by comparing Figs. 27 and 28, we see that the spread is less, at a given time point, when the molecular diffusion coefficient is higher. This is because the effective diffusion coefficient, which incorporates the velocity profile, is higher when the molecular diffusion coefficient is lower. In the unsteady Taylor diffusion limit, as in the steady case, the effective diffusion coefficient has a term that is inversely proportional to the molecular diffusion  $D$ .



**Fig. 27** Propagation of concentration distribution through the Brachial artery;  $D = 0.1 \text{ cm}^2/\text{s}$



**Fig. 28** Propagation of concentration distribution through the Brachial artery;  $D = 10 \text{ cm}^2/\text{s}$

We saw in this section how combining the one-dimensional model we developed with the general (unsteady) Taylor diffusion theory (Azer 2005) is a very useful tool in simulating how an agent present with a given distribution at some time, is dispersed through an artery. Moreover, we saw how the velocity profile which is calculated using the one-dimensional model, is essential in solving this convection-diffusion problem.

## Conclusion and Future Work

In conclusion, we have shown how to combine a one-dimensional model of blood flow with Womersley theory

to include friction without an a priori assumption of velocity profile and to correct the nonlinear terms of the one-dimensional model using the Womersley velocity profiles. We have described a second order algorithm that computes the blood flow in an arterial tree and also the velocity profiles at any location along the tree. Even though the one-dimensional theory and Womersley theory seem at first to be a mismatch, we have shown that they work very well together. The one-dimensional model produces the pressure gradient which the Womersley model needs to calculate velocity profiles and shear stress at the wall. The Womersley model in turn feeds back the computed friction and velocity profiles into the one-dimensional model which is used to produce the flow through the tree. Remarkably, the instantaneous one-dimensional flow and the instantaneous Womersley flow agree to an excellent approximation at every instant of time during the cardiac cycle, throughout the arterial tree. This is true regardless of whether we use the gradient of the static or of the dynamic pressure from the one-dimensional model to drive the Womersley flow, provided only that we enforce a match between the mean flows over time of the two models.

Even though the present results obtained by using the Womersley velocity profile are similar to those of simpler models that assume a particular shape for the velocity profile, other examples of flow in distensible tubes might show greater effects of the velocity profile on the simulated pressure and flow waveforms. One such possibility is in the case of more distensible vessels such as veins, or arteries in certain pathological or disease conditions. Even in situations for which the velocity profile does not have a large influence on the propagation of the arterial pulse, the availability of the velocity profile as output is of great value for comparison with experimental data, such as can be acquired from Doppler Ultrasound. Moreover, the velocity profiles play a central role in the calculation of the effective diffusion coefficient, and convection coefficient, in the theory of time-dependent Taylor diffusion (Azer 2005), as we saw in Sect. “Taylor diffusion combined with blood flow simulation in a vessel”. The effective diffusion coefficient is broken up into two parts, one directly proportional to the molecular diffusion coefficient and one inversely proportional to the molecular diffusion coefficient. The latter term played a significant role in determining the spread of the concentration profile along the axis of the vessel.

In addition, the ability to calculate the shear stress at the wall from a one-dimensional model is important because shear stress plays a vital role in many disease processes. Currently, shear stress can only be calculated from three-dimensional models which are quite expensive computationally, and this makes it only feasible to simulate small three-dimensional sections of the arterial tree. The ability

to compute shear stress using the one-dimensional methods we developed is therefore valuable.

We have compared flow and pressure waveforms obtained from simulations in which the small arteries were modeled by a structured tree approach and by a pure resistance approach. The manner in which we implemented the structured tree was slightly different from (Olufsen et al. 2000). First, at the junction between a large artery and a structured tree, we used the equations of the Riemann invariants along characteristics, which when combined with the convolution condition, gives a quadratic expression for the area that is easily solved, see equation 51. Moreover, within each structured tree, the friction model used was based on Poiseuille flow. The results of the simulations showed that the use of structured trees gives superior pressure and flow waveforms throughout the arterial tree. In particular, these waveforms are far less dominated by reflections than those obtained using pure resistance boundary conditions. An important point is that we were able to see clearly the dicrotic wave in both the flow and pressure waveforms only when the structured tree approach was used.

In order to simulate hypertension, and to distinguish between different theories of hypertension, we have modeled the effect of decreased compliance on pressure waveforms. In our simulation, systolic pressure is increased and diastolic pressure drops slightly with decreased *large* artery compliance, as occurs in isolated systolic hypertension. Diastolic pressure is decreased and systolic pressure increases slightly with decreased *small* artery compliance. The dicrotic wave in the pressure waveform diminishes only when the compliance of the *small* arteries is decreased.

There are several improvements and additions that can be made to the one-dimensional modeling. Arterial segments are typically not constant in diameter, but taper with increasing distance from the heart. Including taper in our one-dimensional model may turn out to increase the effects of the velocity profiles on the nonlinear terms of the one-dimensional equations.

Using the one-dimensional model of arteries and the velocity profiles generated, one can examine the transport of solute in the blood. If a solute is administered at some location and the distribution of solute downstream is desired, then one can use time-dependent Taylor diffusion (Azer 2005), taking advantage of the computed velocity profiles, to calculate the distribution of solute at a particular location downstream from that location (Azer 2006).

In atherosclerosis, it is known that plaques favor branches, bends and bifurcation. Three-dimensional models are typically needed for accurate modeling of flow in these regions, where the three-dimensional geometry is important. A three-dimensional model of a complete arterial

system is not practical, however. One possibility is to employ a three-dimensional model only at bifurcations and bends, and to model the rest of the circulation by means of one-dimensional theory (Dong et al. 2005; Formaggia et al. 2001). The methods of the present paper could be used to incorporate the Womersley profile within the one-dimensional part of such a hybrid model.

In modeling diseases such as hypertension, one has to incorporate other aspects of circulatory dynamics besides the propagation of the arterial pulse. One example is the autoregulation mechanisms for short term and long term regulation of blood pressure. Another example is the kidney's role in regulating blood volume, which in turn has its effects on blood pressure. Adding these components to the current model will lead to a more complete model of the circulation and will provide a more inclusive paradigm for understanding changes in the circulation in disease conditions.

**Acknowledgments** The authors would like to thank Mette Olufsen for helpful discussion on structured trees, and for making available the MRI data of a healthy male subject which was recorded by E.M Pedersen and Y. Kim at Skejby University Hospital in Denmark. This research was supported by the Applied Computer Science Department at Merck & Co., Inc. We would especially like to thank Jeffrey Saltzman, Robert Nachbar and Christopher Tong for their interest in this work and for helpful discussions.

## References

- Azer K. Taylor diffusion in time-dependent flow. *Int J Heat Mass Transfer* 2005;48:2735–40
- Azer K. A one-dimensional model of blood flow in arteries with friction, convection and unsteady Taylor diffusion based on the Womersley velocity profile. Ph.D. thesis, Courant Institute, New York University; 2006
- Calfisch R, Majda G, Peskin CS, Strumolo G. Distortion of the arterial pulse. *Math BioSci* 1980; 229–60
- Caro C, Pedley T, Schroter R, Seed W. The mechanics of the circulation. Oxford University Press; 1978
- Chorin AJ, Marsden JE. A mathematical introduction to fluid mechanics, 3rd ed. New York: Springer; 1998
- Coleman T, Harris J, Guyton A. Whole-body circulatory autoregulation and hypertension. *Circ Res* 1971;XXVIII and XXIX, 76–87
- Courant R, Friedrichs K. Supersonic flow and shock waves. Springer, Applied Mathematical Sciences; 1999
- Dong S, Karniadakis G, Karonis N. Cross-site computations on the teragrid. *Comput Sci Eng* 2005;7(5):14–23
- Feinberg AW, Lax H. Studies of the arterial pulse wave. *Circulation* 1958;XVIII:1125–30
- Formaggia L, Gerbau J-F, Nobile F, Quarteroni A. On the coupling of 3d and 1d Navier-Stokes equations for flow problems in compliant vessels. *Comp Methods Appl Mech Eng* 2001;191(6–7):561–82
- Franklin S. Systolic blood pressure. *Am J Hypertens* 2004;17: 49S–54S
- Griffith T, Klassen P, Franklin S. Systolic hypertension: an overview. *Am Heart J* 2005;149(5):769–75

- Guyton A, Hall J. Textbook of medical physiology. W. B. Saunders Company; 2000
- Hoppensteadt FC, Peskin CS. Modeling and simulation in medicine and the life sciences. 2nd ed. Springer Verlag; 2002
- Iberall A. Anatomy and steady flow characteristics of the arterial system with an introduction to its pulsatile characteristics. *Math BioSci* 1967;197:375–85
- Lax H, Feinberg A, Cohen B. Studies of the arterial pulse wave; the normal pulse wave and its modification in the presence of human arteriosclerosis. *J Chronic Dis* 1956;3(6):618–31
- Mendelsohn M. In hypertension, the kidney is not always the heart of the matter. *J Clin Invest* 2005;115(4):840–4
- Nichols MW, O'Rourke MF. McDonald's blood flow in arteries, theoretical, experimental and clinical principles. 4th ed. Edward Arnold; 1998
- Nichols W. Clinical measurement of arterial stiffness obtained from noninvasive pressure waveforms. *Am J Hypertens* 2005;18:3S–10S
- Olufsen MS, Peskin CS, Kim WK, Pedersen EM, Nadim A, Larsen J. Numerical simulation and experimental validation of blood flow in arteries with structured-tree outflow conditions. *Ann Biomed Eng* 2000;28:1281–99
- Ottesen J, Olufsen M, Larsen J. Applied mathematical models in human physiology. SIAM Monographs on Mathematical Modeling and Computation; 2004
- Pedley TJ. The fluid mechanics of large blood vessels. 3rd ed. Cambridge: Cambridge University Press; 1980
- Richtmeyer, Morton. Difference methods for initial-value problems. 2nd ed. John Wiley and Sons; 1967
- Saltzman J. An unsplit 3d upwind method for hyperbolic conservation laws. *J Comput Phys* 1994;115(1):153–68
- Steele B, Taylor C. Simulation of blood flow in the abdominal aorta at rest and during exercise using a 1-d finite element method with impedance boundary conditions derived from a fractal tree. In: Summer Bioengineering Conference. Summer Bioengineering Conference; 2003
- Stergiopoulos N, Young DF, Rogge TR. Computer simulation of arterial flow with applications to arterial and aortic stenoses. *J Biomech* 1992;25:1477–88
- Taylor G. Dispersion of soluble matter in solvent flowing slowly through a tube. *Proc R Soc Lond Ser A* 1953;219:186–203
- Zamir M. On fractal properties of arterial trees. *J Theor Biol* 1999;197(4):517–26